Study of the Higgs boson properties and search for high-mass scalar resonances in the $H \rightarrow ZZ^* \rightarrow 4\ell$ decay channel at $\sqrt{s} = 13$ TeV with the ATLAS detector

The ATLAS Collaboration

Abstract

The properties of the Higgs boson decaying to four leptons are studied using 14.8 fb^{-1} of integrated luminosity collected in pp collisions by the ATLAS detector at the LHC at a centre-of-mass energy of 13 TeV. The results include measurements of the fiducial cross sections, the different production mode cross sections and a test of beyond the Standard Model interactions using an effective Lagrangian approach. In addition, a search for scalar resonances decaying into the four-lepton final state is performed by exploring the mass range 200-1000 GeV. In all measurements no significant deviation from SM predictions are observed.

1 Introduction

The observation of a new particle in the search for the Standard Model (SM) Higgs boson by the ATLAS and CMS experiments [1, 2] with the data from LHC Run−1 taken during 2011 and 2012 has been an important step towards the clarification of the mechanism of the electroweak (EW) symmetry breaking [3–5]. Further publications by the two experiments from LHC Run−1 have confirmed that the spin, parity and couplings of the new particle are consistent with those predicted for the SM Higgs boson [6–8]. The Higgs boson mass is not predicted by the SM, but once measured the production cross sections and branching ratios can be precisely calculated. The ATLAS and CMS collaborations have reported a combined measurement of the Higgs boson mass of m_H = 125.09 ± 0.21(stat) ±0.11(syst) GeV [9]. This value of the mass is assumed for all Higgs boson analyses reported in this note. A study of the Higgs boson couplings to other SM particles based on the combination of the ATLAS and CMS Run−1 results, has been recently published in Ref. [10].

The Higgs boson decay to four leptons, $H \to ZZ^* \to 4\ell$, where $\ell = e$ or μ, provides good sensitivity for the measurement of its properties due to its high signal-to-background ratio (S/B), which is better than 2 for each of the four final states: $\mu^+\mu^-\mu^+\mu^-$ (4μ), $e^+e^-\mu^+\mu^-$ (2e2μ), $\mu^+\mu^-e^+e^-$ (2μ2e), and $e^+e^-e^+e^-$ (4e), where the first lepton pair is defined to be the one with the dilepton invariant mass closest to the Z boson mass. The largest background for this channel, throughout the four-lepton invariant mass ($m_{4\ell}$) range, is due to continuum $(Z^{(*)}/\gamma^*)(Z^{(*)}/\gamma^*)$ production, referred to as ZZ^* hereafter. For four-lepton events with $m_{4\ell}$ below about 160 GeV there are also non-negligible background contributions from Z + jets and $t\bar{t}$ production with two prompt leptons, where the additional charged lepton candidates arise from decays of hadrons with b- or c-quark content, from π/K in flight decays, from photon conversions or from misidentification of jets.

With the LHC Run−1 data, collected at centre-of-mass energies of $\sqrt{s}$ = 7 and 8 TeV, several measurements were performed in the $H \to ZZ^* \to 4\ell$ channel: coupling and spin/CP measurements, cross section measurements and a search for an additional heavy Higgs boson [11–14]. Preliminary results on $H \to ZZ^* \to 4\ell$ decay channel, based on the first 3.2 fb^{-1} of pp collision data collected at a centre-of-mass energy of 13 TeV have been reported by the ATLAS collaboration in Ref. [15].

This note contains several preliminary results based on the four-lepton final state. The inclusive total and fiducial cross section measurements reported in Ref. [15] are updated including the additional 11.6 fb^{-1} of pp collision data collected in the first 2016 data taking period. In addition the data set is analyzed in terms of the cross section per production mode, using dedicated exclusive event categories and multivariate discriminants. The same categories are used to put constraints on possible beyond the Standard Model (BSM) interactions parameterised in terms of an effective Lagrangian. The BSM scalar and pseudo-scalar interactions of the Higgs boson with the SM vector bosons Z and W boson are investigated. Additional Higgs bosons are predicted by various extensions of the SM Higgs sector, such as the two Higgs doublet model (2HDM) [16] and the electroweak singlet model (EWS) [17]. For this purpose, the $m_{4\ell}$ distribution above 200 GeV is analyzed searching for heavy scalar resonances decaying into the four-lepton final state via a pair of SM Z bosons. Dedicated categories are defined to gain sensitivity to the production mode of such a hypothetical new resonance.

This note is organized as follows. A brief overview of the event selection, with emphasis on updates with respect to Ref. [15], is presented in Section 2. In the same section the strategy adopted for the different measurements reported in this note is outlined. The description of the signal and background samples used in the analyses is given in Section 3. This includes the different production modes of the SM

Higgs boson, the BSM signals derived with the effective Lagrangian approach and the high-mass scalar resonances. The background estimates are reported in Section 4. The modelling of signal and background distributions is reported in Section 5. The systematic uncertainties are discussed in Section 6. The results are summarised in Section 7. Finally the conclusions are given in Section 8.

2 Event selection and analysis strategy

The reconstruction and identification of electrons, muons and jets, as well as the event selection follow closely the strategy described in Refs. [11, 15]. More details on the ATLAS detector and its performance can be found in Ref. [18]. A brief overview on the event selection is given in the following.

Electrons in ATLAS are reconstructed using information from the inner tracking detector (ID) and the electromagnetic calorimeter [19]. Electron candidates are clusters of energy associated with ID tracks, where the final track-cluster matching is performed after the tracks have been fitted with a Gaussian-sum filter [20]. For electrons, background discrimination relies on the shower shape information available from the highly segmented calorimeter, high-threshold transition radiation tracker (TRT) hits, as well as compatibility of the tracking and calorimeter information. This information is combined into a likelihood discriminant. Requirements on the hits in the silicon detectors, including a hit in the innermost layer of the detector, the IBL (or the next-to-innermost layer in case of masked modules), are added. For Run−2, the impact parameter in the transverse plane and its significance ($|d_0|$, and $|d_0|/\sigma_{d_0}$) have been added to the likelihood discriminant, improving the suppression of heavy-flavour background contributions. A "loose" likelihood (LH) selection is applied, which maintains a high efficiency and sufficient background suppression [20]. The electron transverse energy E_T is computed from the cluster energy and the track direction at the interaction point. The cluster energy corrections and calibration are described elsewhere [21]. For the current measurement, the combined fit of the cluster E_T and the track p_T, which was used in Run−1, is not applied.

Muons are reconstructed as tracks in the ID and the muon spectrometer (MS), and their identification is primarily based on the presence of a matching track or tag in the MS [22]. With respect to previous published results, the minimum muon transverse momentum requirement has been lowered from 6 GeV to $p_T > 5$ GeV. This provides an increase in the signal acceptance of about 7% in the 4μ final state. If the ID and MS feature full track information, a combined muon track is formed by a global refit using the hit information from both the ID and MS detectors (combined muons), otherwise the momentum is measured using the ID, and the partial MS track serves as identification (segment-tagged muons). The segment-tagged muons are limited in Run−2 to the centre of the barrel region ($|\eta| < 0.1$) which lacks MS geometrical coverage. Furthermore in this central region, an ID track with $p_T > 15$ GeV is identified as a muon if its calorimetric energy deposition is consistent with a minimum ionizing particle (calorimeter-tagged muons). The muon reconstruction and identification coverage is extended by using tracks reconstructed in the forward region ($2.5 < |\eta| < 2.7$) of the MS, which is outside the ID coverage (standalone muons). For standalone muons, the measurement of the impact parameter is improved by looking for possible hits in the part of the ID closest to the interaction point. The ID tracks associated with muons that are identified inside the ID acceptance are required to have a minimum number of associated hits in each of the ID subdetectors to ensure good track reconstruction. The muon candidates outside the ID acceptance that are reconstructed only in the MS are required to have hits in each of the three MS stations they traverse. At most one standalone or calorimeter-tagged muon is used per event.

The QED process of radiative photon production in Z boson decays is well modeled by simulation. Some of the Final State Radiation (FSR) photons can be identified in the calorimeter and incorporated into the four-lepton measurement. The strategy to include FSR photons into the reconstruction of Z bosons is the same as in Run−1. It consists of a search for collinear (for muons) and noncollinear FSR photons (for both muons and electrons) with only one FSR photon allowed per event.

Jets are reconstructed from clusters of calorimeter cells using the anti-k_t algorithm [23, 24] with a distance parameter $R = 0.4$. The algorithm for the clustering suppresses noise and pileup by keeping only cells with a significant energy deposit and their neighboring cells. The jets are calibrated using a dedicated scheme designed to adjust, on average, the energy measured in the calorimeter to that of the true jet energy. To reduce the number of jet candidates originated from pileup vertices, jets with $p_T < 60$ GeV within the ID acceptance ($|\eta| < 2.4$) have requirements applied to the fraction of tracks which come from the primary vertex [25].

Different objects can be reconstructed from the same detector information, requiring an overlap ambiguity to be resolved. For an electron and a muon which share the same ID track, the muon is selected except for a calorimeter-tagged muon which does not have a MS track or segment-tag in which case the electron is selected. The reconstructed jets which overlap with electrons are removed.

A common preselection is applied for all analyses reported in this note. The data are subjected to quality requirements: if any relevant detector component is not operating correctly during a period in which an event is recorded, the event is rejected. Events are required to have at least one vertex with two associated tracks with $p_T > 400$ MeV, and the primary vertex is chosen to be the reconstructed vertex with the largest $\sum p_T^2$. Four-lepton events are selected and classified according to their final state: 4μ, $2e2\mu$, $2\mu2e$, $4e$.

Four-lepton events are selected with single-lepton, dilepton and trilepton triggers. The electron trigger applies "loose" and "medium" for multilepton triggers or "medium" and "tight" for single-electron trigger likelihood identification, and isolation requirements only in the single-muon triggers. The values of the trigger thresholds used for the 2015 data set are described in Ref. [15]. For the 2016 data the p_T thresholds have been raised and the electron identification tightened with the increase of the peak luminosity during the run. The impact on the signal efficiency is rather small, below 1%. The most affected channel is the 4μ for which the trigger efficiency decreases from 99 to 98% with 2016 trigger thresholds. Globally, the trigger efficiency for signal events passing the final selection is about 99%.

Higgs boson candidates are formed by selecting two same-flavour, opposite-sign lepton pairs (a lepton quadruplet) in an event. The kinematic selection applied to the leptons is the same as the one detailed in Ref. [15] with a few small changes described in the following. In order to cope with the increase of the reducible background due to the lowering of the minimum muon p_T requirement (lowered from 6 to 5 GeV), the four leptons are required to be compatible with the same vertex. A loose χ^2 selection is applied, corresponding to a signal efficiency of 99.5% for all decay channels. The same lepton isolation criteria as applied in Ref. [15] are applied to the leptons in the quadruplets.

Multiple quadruplets within a single event are possible: for four muons or four electrons there are two ways to pair the masses, and for five or more leptons there are multiple ways to choose the leptons. Quadruplet selection is done separately in each sub-channel: 4μ, $2e2\mu$, $2\mu2e$, $4e$, keeping only a single quadruplet per channel. For each channel, the same-flavour opposite-charge lepton pair with the mass closest (second closest) to the Z boson mass is referred to as the leading (subleading) dilepton and its invariant mass is referred to as m_{12} (m_{34}).

The selection criteria that define the signal candidate events are summarized in Table 1.

Table 1: A summary of the event selection requirements.

	Leptons and Jets requirements
	Electrons
	Loose Likelihood quality electrons with hit in innermost layer, $E_{\mathrm{T}} > 7$ GeV and $|\eta| < 2.47$
	Muons
	Loose identification $|\eta| < 2.7$
	Calo-tagged muons with $p_{\mathrm{T}} > 15$ GeV and $|\eta| < 0.1$
	Combined, stand-alone (with ID hits if available) and segment tagged muons with $p_{\mathrm{T}} > 5$ GeV
	Jets
	anti-k_t jets with $p_{\mathrm{T}} > 30$ GeV, $|\eta| < 4.5$ and passing pile-up jet rejection requirements
	Event Selection
Quadruplet Selection	Require at least one quadruplet of leptons consisting of two pairs of same flavour opposite-charge leptons fulfilling the following requirements:
	p_{T} thresholds for three leading leptons in the quadruplet - 20, 15 and 10 GeV
	Maximum of one calo-tagged or standalone muon per quadruplet
	Select best quadruplet to be the one with the (sub)leading dilepton mass (second) closest the Z mass
	Leading dilepton mass requirement: 50 GeV $< m_{12} < 106$ GeV
	Sub-leading dilepton mass requirement: $12 < m_{34} < 115$ GeV
	Remove quadruplet if alternative same-flavour opposite-charge dilepton gives $m_{\ell\ell} < 5$ GeV
	$\Delta R(\ell, \ell') > 0.10$ (0.20) for all same(different)-flavour leptons in the quadruplet
Isolation	Contribution from the other leptons of the quadruplet is subtracted
	Muon track isolation ($\Delta R \leq 0.30$): $\Sigma p_{\mathrm{T}}/p_{\mathrm{T}} < 0.15$
	Muon calorimeter isolation ($\Delta R = 0.20$): $\Sigma E_{\mathrm{T}}/p_{\mathrm{T}} < 0.30$
	Electron track isolation ($\Delta R \leq 0.20$) : $\Sigma E_{\mathrm{T}}/E_{\mathrm{T}} < 0.15$
	Electron calorimeter isolation ($\Delta R = 0.20$) : $\Sigma E_{\mathrm{T}}/E_{\mathrm{T}} < 0.20$
Impact Parameter Significance	Apply impact parameter significance cut to all leptons of the quadruplet.
	For electrons : $|d_0/\sigma_{d_0}| < 5$
	For muons : $|d_0/\sigma_{d_0}| < 3$
Vertex Selection	Require a common vertex for the leptons
	$\chi^2/\mathrm{ndof} < 6$ for 4μ and < 9 for others.

After the FSR correction, the lepton four-momenta of the leading dilepton are recomputed by means of a Z-mass-constrained kinematic fit. The fit uses a Breit-Wigner Z line shape and a single Gaussian per lepton to model the momentum response function with the Gaussian σ set to the expected resolution for each lepton. The Z-mass constraint improves the $m_{4\ell}$ resolution by about 15%. For the high-mass region, the Z-mass constraint is applied to both pairs.

Events satisfying the above criteria are considered candidate signal events for all the described analyses, defining a signal region independent of the value of $m_{4\ell}$. The Higgs boson mass resolution is dependent on the final state and corresponds to 1.6 GeV, 1.7 GeV, 2.1 GeV and 2.4 GeV for 4μ, $2e2\mu$, $2\mu2e$ and $4e$ at $m_H = 125$ GeV, respectively. The strategies for the different measurements and searches on the selected signal candidates are outlined in the following.

2.1 Fiducial cross sections measurement

The selected events in the mass region $115 < m_{4\ell} < 130$ GeV are analyzed to extract the fiducial and total cross sections. The $m_{4\ell}$ distribution is used as a discriminant to increase the sensitivity to the signal. This differs from what was done in Refs. [11, 15] where only event counting was used in the fiducial cross section extraction. The optimal signal mass window ($118 < m_{4\ell} < 129$ GeV) is enlarged when using the $m_{4\ell}$ as a discriminant. The selected candidates in the signal region can be expressed as:

$$
\begin{aligned}
N_{Data}(m_{4\ell})_i = {}& \mathcal{L}_{\text{int}} \cdot \sigma^{\text{tot}} \cdot \mathcal{B}(H \to 4\ell) \cdot \\
& \Big(f_i \cdot PDF(m_{4\ell})_{sig,i} \cdot \sum_{proc} (r_{\text{proc}} \cdot \mathcal{A}_{\text{proc},i} \cdot C_{\text{proc},i}) \Big) + PDF(m_{4\ell})_{bkg,i} \cdot N_{bkg,i}.
\end{aligned}
\tag{1}
$$

where $N_{Data}(m_{4\ell})_i$ is the number of observed data candidates as a function of $m_{4\ell}$ in the decay channel i ($i = 4\mu, 4e, 2e2\mu$ and $2\mu2e$), $\mathcal{L}_{\text{int}}$ the integrated luminosity, σ^{tot} is the total production cross section of the Higgs boson, $\mathcal{B}(H \to 4\ell)$ is the branching ratio of the Higgs boson decay into the four lepton final state, $\mathcal{A}_{proc,i}$ are the acceptance factors (in the fiducial regions defined below) for a given production process (proc = gluon-fusion (ggF), vector boson fusion (VBF), associated production with a Z or W boson (ZH, WH), associated production with a top pair ($t\bar{t}H$)) and decay channel i, and $C_{proc,i}$ are detector correction factors, which account for effects such as trigger, reconstruction and identification efficiencies and reconstruction resolution (again for each production mode and decay channel). $N_{bkg,i}$ is the number of estimated background events per decay channel i. The detector correction factors are estimated from simulation and are given by the ratio of the number of selected reconstructed events relative to the number of particle-level events with Born leptons falling in the fiducial region. They include migration of events into and out of the fiducial region due to resolution effects. The normalised $m_{4\ell}$ distributions are represented by the $PDF(m_{4\ell})$ functions (given separately for each signal final state and for the different backgrounds). The background normalisations and their invariant mass distributions are derived with the methods described in Section 4. The fiducial acceptance factors $\mathcal{A}$ correspond to the theory dependent fraction of $H \to ZZ^* \to 4\ell$ decays that pass the fiducial selection. The r_{proc} parameters represents the fraction of the cross section in a given production process with respect to the total one. The parameters $f_i = \mathcal{B}(H \to i)/\mathcal{B}(H \to 4\ell)$, are the relative branching fraction in each of the four final states. The values of r_{proc} and f_i are taken from the latest available SM calculations [26, 27]. The associated systematic uncertainties are discussed in Section 6.

Table 2: The list of the selections which define the fiducial region of the cross section measurement. Same-flavour opposite-sign lepton pairs are denoted as SFOS, the leading lepton pair mass as m_{12}, and the subleading lepton pair mass as m_{34}.

Lepton definition	
Muons: $p_{\mathrm{T}} > 5$ GeV, $|\eta| < 2.7$	Electrons: $p_{\mathrm{T}} > 7$ GeV, $|\eta| < 2.47$
Pairing	
Leading pair:	SFOS lepton pair with smallest $|m_Z - m_{\ell\ell}|$
Sub-leading pair:	Remaining SFOS lepton pair with smallest $|m_Z - m_{\ell\ell}|$
Event selection	
Lepton kinematics:	Leading leptons $p_{\mathrm{T}} > 20, 15, 10$ GeV
Mass requirements:	$50 < m_{12} < 106$ GeV; $12 < m_{34} < 115$ GeV
Lepton separation:	$\Delta R(\ell_i, \ell_j) > 0.1(0.2)$ for same(opposite)-flavour leptons
J/ψ veto:	$m(\ell_i, \ell_j) > 5$ GeV for all SFOS lepton pairs
Mass window:	$115 < m_{4\ell} < 130$ GeV

In order to minimize the model dependence of the cross section measurement, the fiducial phase space definition follows closely the experimental requirements applied to the four leptons and is summarized in Table 2. The selection is applied at simulation generator level to electrons and muons before they emit photon radiation, referred to as Born-level leptons. No isolation requirement is applied in the fiducial selection, so that any isolation inefficiency is included in C. The small residual model dependence is related to the in and out of acceptance corrections and to the few experimental selection criteria that are not implemented in the fiducial phase space definition (e.g., the lepton isolation criteria).

The values of the acceptance factors ($\mathcal{A}$) and of the correction factors (C) for each production mode and decay channel are summarized in Tables 3 and 4, respectively. The acceptance factors are smaller for the *WH* and *ZH* production modes due to the presence of the additional leptons from vector boson leptonic decays that can be selected in the quadruplet, causing the event to fail the mass window cut. The lower values of the correction factors for the *t̄tH* production mode are due to the presence of several jets that can overlap with the Higgs boson decay leptons.

Table 3: The values of the acceptance factors in % per production mode and decay channel. They are computed for a SM Higgs boson with a mass of 125.09 GeV and a signal mass window of $115 - 130$ GeV.

Acceptance factors $\mathcal{A}[\%]$					
Decay	Production mode				
Channel	ggF	VBF	*WH*	*ZH*	*t̄tH*
4μ	50.9	55.0	43.8	46.5	53.6
$4e$	39.6	43.9	34.4	36.0	44.6
$2\mu 2e$	40.0	42.9	34.0	35.5	42.4
$2e2\mu$	45.9	48.6	38.0	40.4	47.2

The fiducial cross sections can be extracted with a likelihood fit to the observed $m_{4\ell}$ distribution in the signal mass window under different assumptions. The fit is based on the profiled likelihood test statistic under the asymptotic approximation [28]. With the parameterisation described above, the fiducial cross section in each final state can be defined as an independent parameter of interest. The total fiducial cross section can be obtained by defining as parameter of interest the sum of the four final states, without any

Table 4: The values of the correction factors in % per production mode and decay channel. They are computed for a SM Higgs boson with a mass of 125.09 GeV and a signal mass window of $115 - 130$ GeV.

Correction factors $C[\%]$					
Decay	Production mode				
Channel	ggF	VBF	*WH*	*ZH*	$t\bar{t}H$
4μ	62.6	64.2	60.8	60.5	41.8
$4e$	42.1	43.2	43.0	42.7	38.7
$2\mu2e$	46.9	50.9	49.1	48.6	41.7
$2e2\mu$	53.1	54.7	51.8	50.2	36.7

assumption of the relative Higgs boson branching ratios. This approach is referred to as the *sum*. An alternative approach is to combine the four decay channels assuming the relative branching ratios to be those predicted by the SM. This approach is referred to as the *combination*. The first case is less model dependent but it has a slightly reduced statistical sensitivity.

The total inclusive cross section is derived assuming SM values for the Higgs decay branching ratio in the four channels.

2.2 Production mode studies and constraints on κ_{HVV} and $\kappa_{AVV} \cdot \sin \alpha$

In order to gain sensitivity to the different production modes, the events selected in the mass region $118 < m_{4\ell} < 129$ GeV are classified into exclusive categories. The chosen mass range differs from the one used in the fiducial cross section measurement since in the categorisation analysis the mass distribution is not used as a discriminant to allow for the use of jet-based discriminants. The narrower mass range gives better performance when the mass is not used as a discriminant in the fit. Categories based on the presence of additional leptons and the number of jets are used with discriminants optimized to disentangle the different production modes. This categorisation is designed to measure the cross sections per production mode, but it also gives sensitivity to BSM interactions between the Higgs boson and the SM vector bosons W and Z, as described in the following. The schematic flow chart for the event categorisation is shown in Fig. 1.

The events are first categorised in a VH-leptonic category by requiring at least one additional isolated lepton (e or μ) with a transverse momentum greater that 8 GeV. The lepton isolation and transverse impact parameter significance criteria are the same as those applied to the four lepton final state. The events that do not pass this selection are classified into three exclusive categories depending on the number of jets identified in the event. Jets are required to have transverse momentum greater than 30 GeV and a pseudo-rapidity $|\eta| < 4.0$. The categories are 0-jet, 1-jet and 2-jet (where the last one includes events with two or more jets). In the 2-jet category the events are further split into low and high dijet invariant mass. The dijet invariant mass (m_{jj}) is computed with the two highest transverse energy jets. The dijet mass categories are defined by $m_{jj} < 120$ GeV (low-mass) and $m_{jj} > 120$ GeV (high-mass). This further division helps to separate the VH-hadronic (where the vector boson decays to a quark pair) and the VBF production processes. In addition to the event categorisation, a dedicated discriminant is used in each category to improve the sensitivity to the different production modes with the exception of the VH-leptonic one.

For the 0-jet category, a dedicated boosted decision tree (BDT) [29] trained to separate the ggF process from SM backgrounds (dominated by the non-resonant ZZ^* background) is used as in Ref. [11]. This
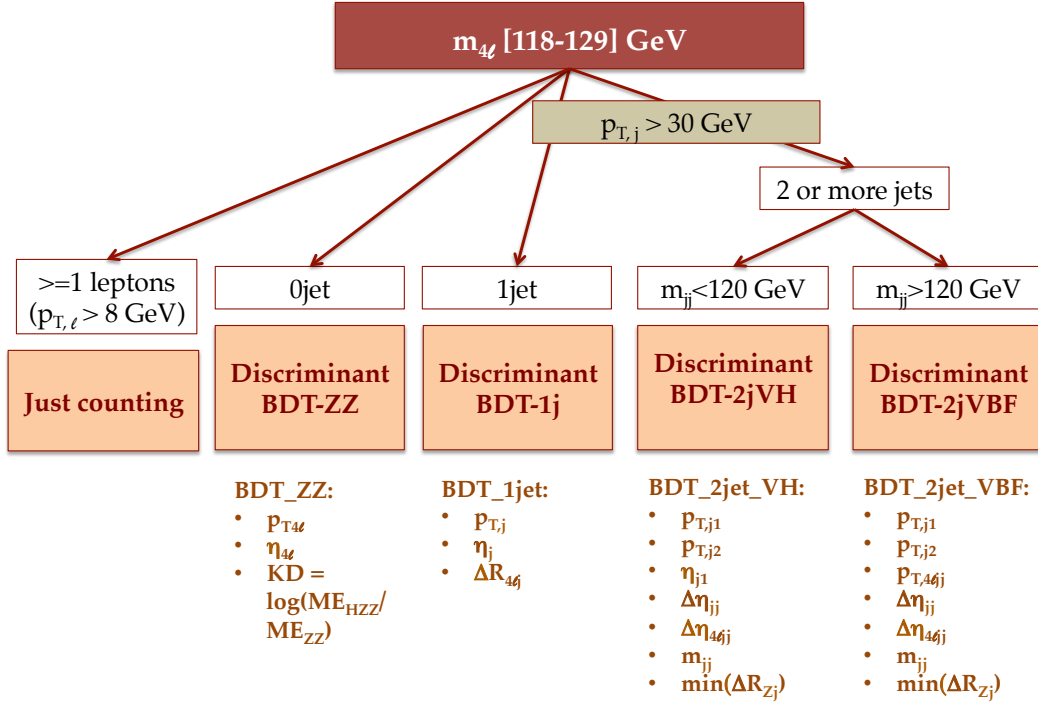
m$_{4\ell}$ [118-129] GeV

p$_{T,j}$ > 30 GeV

2 or more jets

>=1 leptons
(p$_{T,\ell}$ > 8 GeV)

0jet

1jet

m$_{jj}$<120 GeV

m$_{jj}$>120 GeV

Just counting

**Discriminant
BDT-ZZ**

**Discriminant
BDT-1j**

**Discriminant
BDT-2jVH**

**Discriminant
BDT-2jVBF**

BDT_ZZ:
- p$_{T4\ell}$
- $\eta_{4\ell}$
- KD =
  log(ME$_{HZZ}$/
  ME$_{ZZ}$)

BDT_1jet:
- p$_{T,j}$
- η_j
- $\Delta R_{4\ell j}$

BDT_2jet_VH:
- p$_{T,j1}$
- p$_{T,j2}$
- η_{j1}
- $\Delta\eta_{jj}$
- $\Delta\eta_{4\ell jj}$
- m$_{jj}$
- min(ΔR_{Zj})

BDT_2jet_VBF:
- p$_{T,j1}$
- p$_{T,j2}$
- p$_{T,4\ell j}$
- $\Delta\eta_{jj}$
- $\Delta\eta_{4\ell jj}$
- m$_{jj}$
- min(ΔR_{Zj})

Figure 1: A schematic view of the exclusive event categories detailed in the text.

BDT is based on the 4ℓ system pseudo-rapidity, transverse momentum and on the logarithm of ratio of the signal and background matrix elements (the KD discriminant) computed with the lepton kinematics (as detailed in Ref. [11]).

For the 1-jet category a BDT trained to disentangle the ggF production mode from the VBF mode is used. The variables used in this BDT are: the transverse momentum ($p_{T,j}$) and the pseudorapidity (η_j) of the jet and the angular separation between the four-lepton system and the jet ($\Delta R_{4\ell j}$).

Similarly, for the 2-jet categories two BDTs trained to disentangle the ggF production mode from the VH-hadronic and from the VBF mode are used in the low-mass and high-mass category, respectively. The BDT used in the high-mass category is based on the following variables: the jet transverse momenta ($p_{T,j1}$ and $p_{T,j2}$), the dijet invariant mass (m_{jj}), the pseudorapidity separation ($\Delta\eta_{jj}$) of the two leading jets, the transverse momentum of the di-jet plus four-lepton system ($p_{T,4\ell jj}$), the minimum angular separation between the leading dilepton pair and the two leading jets (min(ΔR_{Zj})) and the difference in pseudorapidity between the four-lepton system and the average pseudorapidity of the two leading jets ($\Delta\eta_{4\ell jj}$). For the low-mass category the same variables are used with the exception of the $p_{T,4\ell jj}$(this variable brings little improvement in the low-mass category).

This experimental categorisation also provides sensitivity to possible BSM interactions. In particular, BSM interactions between the Higgs boson and the SM vector bosons W and Z would have a large im-

pact on the yields in the VH and VBF production modes since they would modify simultaneously the production and the decay interactions. In order to study these interactions the BSM effects are parameterised following the Higgs characterization model described in Ref. [30]. Only the effective Lagrangian terms related to the BSM couplings κ_{HVV} and κ_{AVV} of Equation 2.2 of Ref. [30] are considered in this note as in previous ATLAS studies [12], where, however, these interactions were considered only in the Higgs boson decay. They describe BSM scalar (κ_{HVV}) and pseudo-scalar (κ_{AVV}) interactions between the Higgs boson and the Z and W SM vector bosons. The BSM couplings are assumed to be the same for the W and Z bosons (i.e., $\kappa_{HVV} = \kappa_{HZZ} = \kappa_{HWW}$ and $\kappa_{AVV} = \kappa_{AZZ} = \kappa_{AWW}$). The scale of the new physics described in the model (Λ) is fixed at 1 TeV and the coupling that describes the SM-like interaction is fixed to the SM value ($\kappa_{SM} \cdot \cos \alpha = 1$ of Ref [30]). For the BSM scalar interaction the value of $\cos \alpha$ of Ref. [30] is fixed to 1, so that the interaction is described by the single parameter κ_{HVV}. For the pseudo-scalar interaction the coupling of the BSM part is defined as a single parameter $\kappa_{AVV} \cdot \sin \alpha$ of Ref. [30]. With these assumptions and this parameterisation, the interactions between the Higgs boson and the vector bosons are the same as in the SM when the value of the BSM coupling is zero.

In order to study the impact of the BSM interactions on the experimental categories, BSM samples have been generated using the code MADGRAPH5_AMC@NLO [31] and are used to emulate different values of the couplings using a morphing technique described in Section 5. The data yields are fit to the expected BSM signal in each category, without the use of discriminants. The SM-like part of the interaction is fixed to the predictions by the latest SM calculations [26, 27].

2.3 High-mass analysis

The signal candidate events selected in the invariant mass region above 140 GeV are used to search for heavy scalar resonances decaying via the process $ZZ \rightarrow 4\ell$. The analysis is close to the one described in Ref. [15]. The basic event selection is described in section 2 with the addition of the Z-mass constraint applied to both dilepton pairs, as both Zs are expected to be on-shell.

A few improvements with respect to Ref. [15] are implemented in this study: in addition to the inclusive search, categories sensitive to ggF and VBF production modes are added. An event is classified as originating from the VBF production mode if there are two or more jets in the event, the invariant mass of the di-jet system is above 400 GeV and the jets are well separated in η ($|\Delta\eta| > 3.3$). Otherwise the event enters the ggF category.

The results are expressed as 95% confidence upper limits derived separately for ggF and VBF production cross sections of the additional heavy Higgs-like boson assuming the Narrow Width Approximation (NWA). In the case of the NWA, the heavy Higgs boson is modelled with a Breit-Wigner with a fixed width of 4.07 MeV as predicted for the SM Higgs boson with a mass of 125 GeV. Under the NWA assumption, the interference of a light Higgs with the gg-initiated ZZ continuum can be safely ignored. The modelling of the signal and background used for the high-mass analysis is discussed in Section 5.

In addition to the NWA, the case of a signal with Large Width Approximation (LWA) is also studied, as several theoretical models favor this hypothesis. In this case the signal is modelled with a Breit-Wigner with a width varying up to 10% of its mass. Results for a heavy Higgs boson with a width of 1%, 5% and 10% of its mass are presented. The interference with the SM background is found to be small and therefore is neglected. In the LWA analysis, no categories (sensitive to ggF and VBF production modes) are used.

3 Signal and background simulation

The production of the SM Higgs boson is modelled using the POWHEG-BOX v2 Monte Carlo (MC) event generator [32, 33], which calculates separately the ggF and VBF production mechanisms with matrix elements up to next-to-leading order (NLO) in QCD. POWHEG-BOX is interfaced to PYTHIA 8 [34] for showering and hadronization, which in turn is interfaced to EvtGen v1.2.0 [35] for the simulation of b and c-hadron decays. The $H \rightarrow ZZ^* \rightarrow 4\ell$ decay is also performed in PYTHIA 8. In addition, a ggF sample modelled with MadGraph5_aMC@NLO is used for systematics studies. This includes up to two additional jets at NLO QCD accuracy with the FxFx merging scheme [31, 36].

PYTHIA 8 is used to simulate the production of a Higgs boson in association with a W or a Z boson. The production of a Higgs boson in association with a top quark pair is simulated using MadGraph5_aMC@NLO [31] and is interfaced to Herwig++ [37] for showering and hadronization.

The Higgs boson production cross sections[1] and decay branching ratios, as well as their uncertainties, are taken from Refs. [26, 27, 38–68]. Table 5 summarises the production cross sections and branching ratios for $H \rightarrow ZZ^* \rightarrow 4\ell$ at 13 TeV for $m_H = 125.09$ GeV .

Table 5: The predicted SM Higgs boson production cross sections (σ) for ggF, VBF and associated production with a W or Z boson or with a $b\bar{b}$ or $t\bar{t}$ pair in pp collisions for $m_H = 125.09$ GeV at $\sqrt{s} = 13$ TeV [26, 27, 38–68]. The quoted uncertainties correspond to the total theoretical systematic uncertainties calculated by adding in quadrature the QCD scale and PDF+α_s uncertainties. The decay branching ratio ($\mathcal{B}$) with full uncertainty for $H \rightarrow ZZ^* \rightarrow 4\ell$ with $\ell = e, \mu$, is also given.

$\sigma (gg \rightarrow H)$ pb	$\sigma (qq' \rightarrow Hqq')$ pb	$\sigma (q\bar{q}' \rightarrow WH)$ pb	$\sigma (q\bar{q}/gg \rightarrow ZH)$ pb
48.5 ± 2.4	3.78 ± 0.08	1.369 ± 0.028	0.88 ± 0.04

$\sigma (q\bar{q}/gg \rightarrow t\bar{t}H)$ pb	$\sigma \left(q\bar{q}/gg \rightarrow b\bar{b}H \right)$ pb	$\mathcal{B}(H \rightarrow ZZ^* \rightarrow 4\ell)$ $[10^{-4}]$
0.51 ± 0.05	0.49 ± 0.12	1.250 ± 0.027

Additional VBF and VH signal samples with different values of the BSM couplings κ_{HVV} and $\kappa_{AVV} \cdot \sin \alpha$ have been generated with MadGraph5_aMC@NLO at leading order in QCD and are used for the signal morphing as a function of the BSM couplings as explained in Section 5.

For the high-mass scalar search, ggF and VBF samples for different values of the mass of the scalar and with a narrow width of 4.07 MeV as predicted in the SM for $m_H = 125.09$ GeV, have been generated with POWHEG-BOX. The mass range is between 200 GeV to 1 TeV in steps of 100 GeV. In addition, ggF samples with a width of 5% and 10% of the scalar mass m_S have been generated with MadGraph5_aMC@NLO.

The ZZ^* continuum background from quark-antiquark annihilation is modelled at NLO in QCD using POWHEG-BOX v2 and interfaced to PYTHIA 8 for parton shower and hadronization, and to EvtGen v1.2.0. The CT10NLO [69] set is used as Parton Density Function (PDF) of the hard process while the CTEQL1 PDF set is used for the parton shower. The non-perturbative effects are modelled using the AZNLO [70] tune. NNLO QCD and NLO EW corrections are considered for the quark-initiated ZZ^* [71–

---

[1] For the ggF production mode the prediction with the N^3LO accuracy in QCD is used.

73] as function of m_{ZZ^*}. In addition, a ZZ^* sample simulated with the SHERPA 2.1.1 generator has been used for systematics studies. This sample includes matrix elements for up to 1 parton at NLO and up to 3 partons at LO.

The gluon induced ZZ^* production, for high m_{ZZ^*}, is modelled by SHERPA 2.1.1 [74], which includes also the off-shell Higgs boson signal and their interference. For low m_{ZZ^*} GG2VV [75] has been used. The k-factor accounting for higher order QCD effects for the $gg \rightarrow ZZ^*$ continuum production has been calculated for massless quark loops [76, 77] in the heavy top-quark approximation [78], including the $gg \rightarrow H^* \rightarrow ZZ$ processes [79]. Based on these studies, a k-factor of 1.7 is used, and a conservative relative uncertainty of 60% on the normalization is applied to the m_{ZZ^*} distribution.

The WZ background is modelled using POWHEG-BOX v2 interfaced to PYTHIA 8 and EVTGEN v1.2.0. The triboson backgrounds ZZZ, WZZ, and WWZ with four or more prompt leptons are modelled using SHERPA 2.1.1. For the fully leptonic $t\bar{t} + Z$ background, with four prompt leptons coming from the top and Z decays, MADGRAPH5_AMC@NLO is used.

Events containing Z bosons with associated jets are simulated using the SHERPA 2.2.0 generator. Matrix elements are calculated for up to 2 partons at NLO and 4 partons at LO using the COMIX [80] and OPENLOOPS [81] matrix element generators and merged with the SHERPA parton shower [82] using the ME+PS@NLO prescription [83]. The CT10 PDF set is used in conjunction with dedicated parton shower tuning developed by the SHERPA authors. The Z + jets events are normalised to the NNLO cross sections.

The $t\bar{t}$ background is modelled using POWHEG-BOX v2 interfaced to PYTHIA 6 [84] for parton shower, fragmentation, and the underlying event and to EVTGEN v1.2.0 for properties of the bottom and charm hadron decays.

Generated events are processed through the ATLAS detector simulation [85] within the GEANT4 framework [86]. Additional pp interactions in the same and nearby bunch crossings (pileup) are included in the simulation. The simulation samples are weighted to reproduce the observed distribution of the mean number of interactions per bunch crossing in the data.

4 Background estimates

The main background component in the $H \rightarrow ZZ^* \rightarrow 4\ell$ final state is the non-resonant ZZ^* production which is modelled using simulation normalised to the SM predictions, as described in Section 3. Additional background sources are the Z+jets and $t\bar{t}$ processes which are estimated in the signal region using different data-driven techniques according to the flavour of the sub-leading lepton pairs ($\mu\mu$ or ee). The estimation of these backgrounds follows the methods described in [15] with a few small modifications described in the following. The WZ production is included in the data-driven results for the $\ell\ell + ee$ final states, while it is added from simulation for the $\ell\ell + \mu\mu$. The contributions from $t\bar{t}V$ and triboson processes are minor and taken from simulation.

4.1 $\ell\ell + \mu\mu$ background

The $\ell\ell + \mu\mu$ background is estimated using the shape of the leading dilepton invariant mass m_{12} in three Control Regions (CRs) where each CR is enriched in a different component ($t\bar{t}$, Z+heavy-flavour, Z+light-flavour) and extrapolated to the signal region using transfer factors.

In a first step, the relative normalisation of the $t\bar{t}$ and Z+heavy-flavour is obtained with an unbinned maximum-likelihood simultaneous fit of the m_{12} spectrum in two orthogonal CRs:

- the *inverted-d_0 CR*, enriched in Z+heavy-flavour, which has a same-flavour leading di-lepton pair passing the analysis requirements and has the transverse impact parameter significance cut inverted and no isolation requirements on the subleading muon pair.

- the *$e\mu+\mu\mu$ CR*, enriched in $t\bar{t}$, in which a different-flavour leading dilepton pair passing the analysis requirements is accompanied by a subleading dimuon pair without the isolation, transverse impact parameter significance nor charge selections applied.

For the $t\bar{t}$ component the m_{12} distribution is modeled by a second-order Chebyshev polynomial, while for the Z+jets component it is modeled using a convolution of a Breit-Wigner distribution with a Crystal Ball[2] function. The result of the simultaneous fit is shown in Figure 2(a) and Figure 2(b).

The Z+light-flavour component with subleading muons mainly coming from π/K decays in-flight is determined in a second step by fitting the m_{12} distribution in a third CR (denoted *inverted isolation CR*) where at least one of the subleading muons fails the isolation cut used in the analysis. The amount of the Z+heavy-flavour and $t\bar{t}$ components is constrained, within the uncertainties, to the result of the simultaneous fit in the $e\mu + \mu\mu$ CR and *inverted-d_0 CR*. The result of the fit is show in Figure 2(c). In both steps, the small contribution of ZZ^* and WZ is estimated from simulation.

The estimates for the first two components are expressed in terms of yields in a validation region (denoted *relaxed CR*) defined by applying the analysis event selection except for the isolation and impact parameter significance requirements to the subleading dimuon pair.

Finally, the three background components are extrapolated from the control regions to the signal region using simulated samples. The isolation and impact parameter significance simulation-based efficiencies are validated with data using a $Z + \mu$ control sample and the corresponding differences between data and simulation are taken as systematic uncertainties in the transfer factors. Table 6 shows the yields estimated in the *relaxed CR* for Z+heavy-flavour jets and $t\bar{t}$, and the *inverted-isolation CR* for Z+light-flavour jets backgrounds. The transfer factors used to extrapolate the fitted yields from the control to the signal region and the final estimate in the signal region for the three background components are also shown. The transfer factors are estimated with MC simulation for each background component and are quoted in this table with their statistical uncertainty from the MC sample. For Z+light-flavour jets, a 10% systematic uncertainty is assigned which corresponds to the difference seen in data and MC simulation in the isolation efficiency.

4.2 $\ell\ell + ee$ background

The main background in the $\ell\ell + ee$ process arises from the misidentification of light-flavour jets as electrons (denoted as f), photon conversions (denoted as γ) and the semi-leptonic decays of heavy-flavour hadrons (denoted as q). The estimation of the electron background (for f and γ) is extracted from a control region, denoted as $3\ell+X$, where the first three leptons pass the full analysis selection, but the identification criteria for the lower p_T electron in the subleading pair (denoted with X) are relaxed. X is only required to have a minimum number of hits in the ID and the same charge as the other subleading electron. The heavy flavour component has a small contribution to the $3\ell+X$ CR and is estimated from simulation.
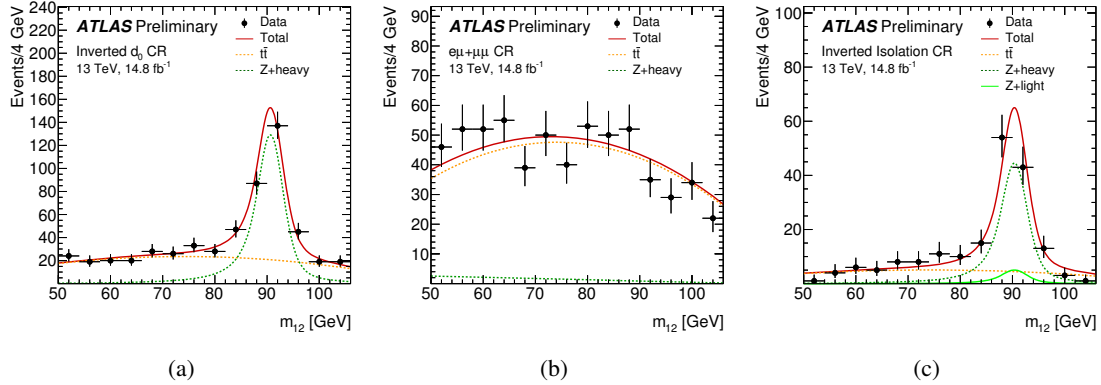
---

[2] a Gaussian core with a power law tail

Figure 2: The distributions of m_{12} for data in the three CRs used for the $\ell\ell + \mu\mu$ background estimate. The result of the simultaneous fit to the data (continuous line) for the inverted-d_0 and the $e\mu + \mu\mu$ CRs is shown in (a) and (b). The fit to data of the inverted-isolation CR is shown in (c). The dashed lines correspond to the Z+jets (green) and $t\bar{t}$ (yellow) components of the fit, where for (c) the Z+light jets has been fit with the Z+heavy yield scaled to the result of the simultaneous fit of the other two CRs.

Table 6: The fitted yield estimated in the *relaxed CR* for Z+heavy-flavour jets and $t\bar{t}$, and the *inverted-isolation CR* for Z+light-flavour jets backgrounds in the $\ell\ell + \mu\mu$ final states for 14.8 fb^{-1} at $\sqrt{s}$ = 13 TeV. The corresponding extrapolation factors and signal region yields are also given. The uncertainties on the fit yields are statistical. Those on the extrapolation factors are derived from the simulation sample size and contribute to the systematic uncertainty on the SR yields. The statistical and systematic uncertainties are given for the extrapolated SR yields.

Background	Fit yield in CR	Extrapolation factor [%]	Yield in SR
Z+heavy-flavour jets	348 ± 29	(0.60 ± 0.04)	$2.10 \pm 0.17 \pm 0.13$
$t\bar{t}$	351 ± 14	(0.21 ± 0.03)	$0.74 \pm 0.03 \pm 0.00$
Z+light-flavour jets	10 ± 15	(2.3 ± 0.3)	$0.24 \pm 0.35 \pm 0.03$
WZ	(MC-based estimation)		0.63 ± 0.31

Each source of background has different properties and efficiency, therefore the target of the background estimation method is to disentangle the components with suitable discriminating variables. In MC simulation, the actual origin is known and is extracted using truth information. For data, the various components are unfolded directly using a template fit on the number of innermost (or next-to-innermost)[3] pixel hits of the track associated to the lepton (n_{InnerPix}). The distribution of n_{InnerPix} for events falling into this control region is fitted with templates which characterize the γ and f backgrounds in order to extract the yields of each component. The templates, shown in Figure 3(a), are obtained from MC simulation from the $Z + X$ CR; small corrections are applied to the templates for γ and f in order to better describe the data. The small contribution of the ZZ^* with a charge flip and heavy-flavour electrons in the $3\ell+X$ CR are subtracted from the fit result according to the expectation. Figure 3(b) shows the result of the fit performed on data combining the $2\mu2e$ and $4e$ channels. The efficiency to estimate the SR background from the CR for f and γ is taken from simulation and corrected to data using the enriched $Z+X$ CR samples. In Table 7 the estimation of each background component in the SR together with the yield from the data fit and the efficiency averaged over p_{T} is shown. The dominant uncertainties are systematic and come from

---

[3] A hit in the next-to-innermost pixel layer is used when the innermost pixel layer module is not working.

the precision on the selection efficiencies obtained from the Z+X sample for the f and γ estimates and from the MC-based estimation for the heavy-flavour component.
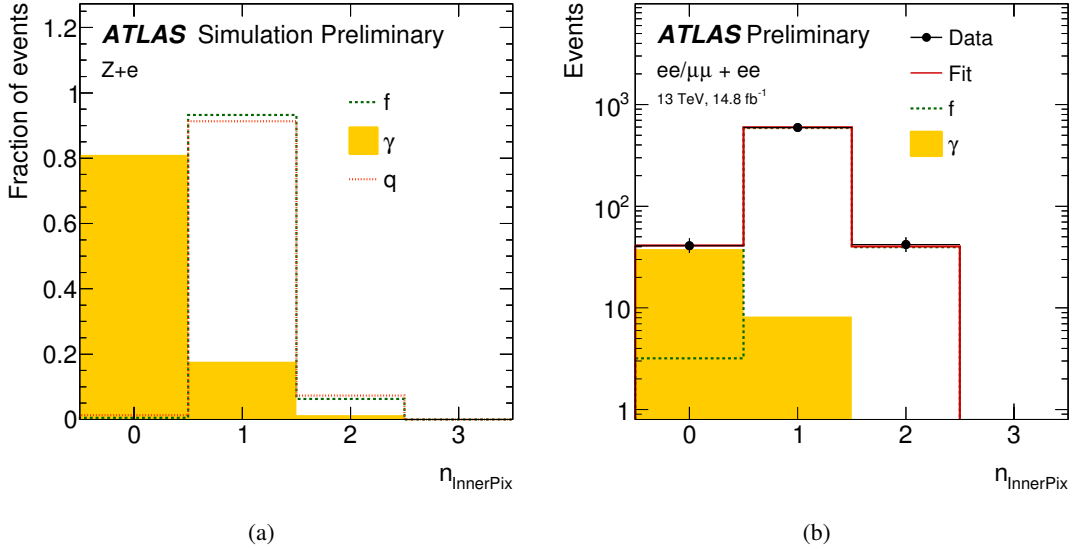

(a)   (b)

Figure 3: (a) The templates used in the 3l+X fit to the number of innermost pixel hits n_{InnerPix} for the different sources of background : γ and f which are extracted from MC simulation in the Z+X control sample and corrected using data. (b) The data $3\ell+X$ events and result of the fit to n_{InnerPix}, combining $2\mu 2e$ and $4e$ channels. The fit components modeling f and γ contributions are also shown.

Table 7: The fit results for the yields in the $3\ell+X$ CR for 14.8 fb^{-1} at $\sqrt{s} = 13$ TeV with statistical errors, shown together with the efficiency used to extrapolate the yields to the SR. The SR yields for the f and γ components are quoted with the statistical uncertainty as returned from the data fit and a systematic uncertainty coming from the efficiency and the fit. For the q component the SR yield is evaluated directly from simulation and is quoted with its total uncertainty.

type	data fit	efficiency [%]	SR yield
f	1228 ± 35	0.23 ± 0.03	$2.62 \pm 0.08 \pm 0.36$
γ	79 ± 10	0.76 ± 0.05	$0.55 \pm 0.08 \pm 0.04$
q	(MC-based estimation)		2.50 ± 0.77

4.3 Shape of the reducible background contribution and the estimates for the categories

The $m_{4\ell}$ distribution of the reducible backgrounds is required for the normalisation and shape of these backgrounds in the different fit regions used in the analysis. The shape of the distribution is taken from the Z+jets and $t\bar{t}$ simulation and it is smoothed using the kernel density estimation method [87]. The same shape is used for all channels while the difference seen among $\ell\ell + ee$ and $\ell\ell + \mu\mu$ final state is taken as the systematic uncertainty. The shape of the background in the $m_{4\ell}$ distribution extrapolated to the signal region can be seen in Fig. 4(a) and 5(a).

15

The fraction of events falling in a given category with respect to the inclusive yield of simulated Z+jets and $t\bar{t}$ processes is used to scale the data-driven estimate. The shape of the reducible backgrounds for a given observable is also taken from MC simulation, relaxing the isolation selections to enhance the statistics. The dominant uncertainty in this procedure is coming from the MC statistics, which is taken into account. Applying these fractions to the data-driven inclusive background estimates described above yields the reducible background estimates per category for each production mode shown in Table 12.

5 Signal and background modeling

5.1 Modeling for the Higgs boson cross section and production mode studies

As mentioned in Section 2, the observable used for the signal extraction of the Higgs cross section is the invariant mass of the four-lepton system in the range 115-130 GeV. The $m_{4\ell}$ shape for the signal and the ZZ^* background is taken from simulation. For the reducible backgrounds, the shape is obtained as described in Section 4.

For the measurement of the Higgs production modes, the shapes of the BDTs are predicted using simulation for both the signal and the ZZ^* background. The fraction in each category used in the analysis is also obtained from simulation. For the reducible backgrounds, the shapes of the BDT discriminant output as well as the yields in the different categories are obtained as explained in Section 4.

5.2 Signal modeling for the study of the BSM couplings κ_{HVV} and $\kappa_{AVV} \cdot \sin \alpha$

Yields in the event categorisation introduced in Section 2 are also sensitive to BSM interactions in the HZZ vertex. In order to obtain a continuous signal parameterisation for all of the physical observables like the cross sections or the differential distributions as a function of the BSM coupling parameters, a morphing technique has been used [88].

The morphing-based signal model of an observable O with a given set of BSM couplings $\vec{g}_{\text{target}} \equiv \{g_{\text{SM}}, g_{\text{BSM},1}, .., g_{\text{BSM},n}\}$ is obtained as

$$O_{\text{out}}(\vec{g}_{\text{target}}) = \sum_i w_i(\vec{g}_{\text{target}}, \vec{g}_i) \cdot O(\vec{g}_i) \tag{2}$$

which corresponds to a linear combination of a minimal set of base samples (templates) with couplings $\vec{g}_i = \{g'_{\text{SM},i}, g'_{\text{BSM},1}, .., g'_{\text{BSM},n}\}$ spanning the full coupling parameter space. The weight of each template is derived from the coupling parameters appearing in the signal matrix element. For a calculation at the lowest order and with the narrow-width approximation assumption, this yields a second order polynomial for both the production and decay. In this analysis, only the presence of one BSM coupling among $\kappa_{AVV} \cdot \sin \alpha$ and κ_{HVV} is considered at a time. Since in the ggF and ttH production modes the interaction between the Higgs boson and the vector bosons is present only in the decay while for the VH and VBF the interaction is both in the production and decay, three independent samples are needed to form a morphing base sample set in the former case, while five samples are needed for the latter. The value of the BSM couplings for the samples used to build a base sample set for the signal morphing as a function of $\kappa_{AVV} \cdot \sin \alpha$ and κ_{HVV}, respectively, has been chosen to ensure a reasonably small statistical uncertainty of any target sample with BSM couplings within the range under study.

Since the total width for the generated samples is kept fixed to the SM value, an additional correction, corresponding to $\Gamma_{\text{BSM}}/\Gamma_{\text{SM}}$, is applied to the $\sigma \cdot \mathcal{B}(H \to ZZ)$ for the samples with non-zero value for BSM couplings. The correction is of the order of -2% for $\kappa_{AVV} \cdot \sin\alpha = \pm 8$ and is about $+14\%$ and -17% for $k_{HVV} = -8$ and $k_{HVV} = +8$, respectively. For the ggF case, only the branching ratio modification is considered in the morphing while the change of the acceptance in the analysis categories as a function of the BSM coupling parameters is small and thus neglected.

5.3 Modeling for the high-mass scalar search

In the case of a narrow width resonance, the reconstructed four lepton invariant mass is determined essentially by the detector resolution. A sum of a Crystal Ball function and a Gaussian is used to describe the $m_{4\ell}$ shape of a heavy scalar with a narrow width, as described in [15]. This signal parameterisation is used for both ggF-enriched and VBF-enriched categories.

The bias on the signal yield extraction introduced by using the analytical function is below 1.5%. The function parameters are described separately for each final state as a function of the scalar mass, m_S with first- and second-degree polynomials. The use of this parameterisation for the function parameters introduces an extra bias on the signal yield and m_S extraction of about 1%.

The signal acceptance, which includes the reconstruction efficiency, is parameterised as a function of the m_S with a second-degree polynomial separately for the 4μ, $4e$ and $2e2\mu$ final states and for both ggF and VBF production modes in the experimental ggF-enriched category. For the VBF-enriched category, events are not further categorised according to their final state. The acceptance values for ggF and VBF production modes in the ggF-enriched and VBF-enriched categories for two reference m_S values are illustrated in Table 8.

Table 8: The values of the acceptance in % for m_S=300 GeV and 800 GeV ggF and VBF signals in the four experimental categories used in the high mass scalar search: the 4μ, $4e$, $2e2\mu$ (ggF-enriched) and the VBF-enriched.

| | signals | | | |
category	300 GeV ggF	300 GeV VBF	800 GeV ggF	800 GeV VBF
4μ ggF-enriched	14.3	9.1	16.4	9.9
$4e$ ggF-enriched	10.7	6.8	14.0	8.7
$2\mu2e$ ggF-enriched	24.6	16.0	30.5	18.9
VBF-enriched	1.8	22.2	4.0	29.0

For the case of the LWA, the $m_{4\ell}$ shape is described as a convolution of the truth distribution with a resolution function. Resolution effects can be described by the NWA parameterisation described previously, since the NWA $m_{4\ell}$ shape has negligible truth structure and is completely dominated by detector effects.

For the high-mass scalar search, the $m_{4\ell}$ shapes for the $q\bar{q} \to ZZ$ and $gg \to ZZ$ background are parameterised in all the four analysis categories with the same analytical function

$$f_{qqZZ/ggZZ}(m_{4\ell}) = (f_1(m_{4\ell}) + f_2(m_{4\ell})) \times H(m_{4\ell} - m_0) \times C_0 + f_3(m_{4\ell}) \times H(m_0 - m_{4\ell}) \qquad (3)$$

where:

$$f_1(m_{4\ell}) = \exp(a_1 + a_2 \cdot m_{4\ell})$$
$$f_2(m_{4\ell}) = (\frac{1}{2} + \frac{1}{2}erf(\frac{m_{4\ell} - b_1}{b_2})) \times \frac{1}{1 + \exp(\frac{m_{4\ell}-b_1}{b_3})}$$
$$f_3(m_{4\ell}) = \exp(c_1 + c_2 \cdot m_{4\ell} + c_3 \cdot m_{4\ell}^2 + c_4 \cdot m_{4\ell}^{2.7})$$
$$C_0 = \frac{f_3(m_0)}{f_1(m_0) + f_2(m_0)}$$

(4)

The first part of the function f_1 takes care of the flat low mass part of the spectrum where one of Z bosons is off-shell, while f_2 models the ZZ threshold around $2 \cdot m_Z$ and f_3 describes the high mass tail. The transition between low mass and high mass parts is done by the Heaviside step function $H(x)$ around $m_0 = 240$ GeV. The continuity of the function around m_0 is insured by normalisation factor C_0 that is applied to the low mass part. Finally, a_i, b_i and c_i are shape parameters which are obtained by fitting the simulated $m_{4\ell}$ for each final state.

6 Systematic uncertainties

The systematic uncertainties in this analysis can be divided into experimental and theoretical systematic uncertainties. The first category includes uncertainties on the modeling of the physics objects (leptons and jets reconstruction, identification efficiencies, energy resolution and scale) and on the total integrated luminosity. Uncertainties on the procedure used to derive the data-driven background estimates are also included in this category. The second category includes uncertainties on the modeling of the signal and the background processes.

In both cases, the uncertainties are implemented in the analyses by means of nuisance parameters (NP) in the profile likelihoods [28] used to extract the measurements reported in this note. The uncertainties can act on the signal acceptance, efficiency and discriminant distributions as well as on the background estimates. If the same source of uncertainty affects both signal and backgrounds, the corresponding NP is correlated in the fit (e.g., the error on the integrated luminosity can affect the signal cross-section and the MC-based background estimates). A NP can change the signal efficiency and acceptance as well as the discriminant distributions for the signal and background processes.

6.1 Experimental uncertainties

The lepton identification and reconstruction efficiencies and energy/momentum scale and resolution are derived from data using large samples of $J/\psi \to \ell\ell$ and $Z \to \ell\ell$ decays. The uncertainties on the muon performance are computed following the procedure reported in Ref. [22] and the electron performance uncertainties are derived following the method described in Refs. [20, 89]. Typical uncertainties on the identification efficiencies are in the range between $0.5 - 1.0\%$ for muons and $1.0 - 1.3\%$ for electrons. The uncertainty on the electron and muon energy scale and resolution are small and have a negligible impact on the analyses reported in this note.

For jets, the systematic uncertainties are derived following the procedure described in Ref. [90]. These uncertainties only affect the measurements based on the event categories described in Section 2.2 and the high-mass search for the results given separately in the ggF and VBF categories. All other analyses are inclusive in the number of jets and therefore are not affected by the correspondent systematic uncertainty. The transverse jet energy scale and resolution uncertainties are in the range $3-7\%$ and $2-4\%$, respectively [91]. The measurement that is most affected by this systematics is the cross section of the VBF production mode. The impact of the jet uncertainties on the VBF cross section are of the order of 15%.

The uncertainty on the integrated luminosity has been derived following the method described in Ref. [92, 93], based on beam-separation measurements (also known as Van der Meer scans). The relative uncertainty for the 2015 data set is 2.1% while for the 2016 data set is 3.7%.

The reducible backgrounds are estimated using data-driven techniques, as detailed in Section 4. Their estimates are extracted with a precision of 14% for $\ell\ell + ee$ and 14% for the $\ell\ell + \mu\mu$ final states. The larger uncertainty in the $\ell\ell + \mu\mu$ final states comes from the limited statistics in extracting the simulation-based extrapolation factor for the Z+light-flavour jet component. In addition to the error on the yield for the different experimental categories, uncertainties are also derived for the distributions of the discriminants used in the different analyses.

The precision of the Higgs boson mass measurement as obtained from the ATLAS-CMS combination, $m_H = 125.09 \pm 0.24$ GeV [9], has been taken into account in the systematic uncertainties. It can affect the signal extraction via the mass distribution in the total cross section measurement or the mass window acceptance for the categorised signal extraction.

6.2 Theoretical uncertainties

The theoretical uncertainties can impact the measurements reported in this note in several ways. In the following each measurement is discussed separately.

6.2.1 Theoretical uncertainties in fiducial and total inclusive cross sections

For the fiducial cross sections the theoretical uncertainties can impact the determination of the correction factors, in particular the production mode fractions r_{proc}, which are based on the best available SM calculations, and the background estimates. In order to avoid model dependence, but taking into account existing constraints from measurements, the uncertainties on the production mode fractions are taken from the ATLAS-CMS combined couplings measurement [10]. They amount to about 30%, 90% and 100% for the VBF, VH and $t\bar{t}H$ processes, respectively. The relative impact of these uncertainties on the correction and acceptance factors is at the level of 1% and 0.4%, respectively.

The uncertainty on the expected ZZ^* background, evaluated by varying the QCD normalisation and factorization scales, varies with m_{ZZ^*}, from ± 3 to $\pm 5\%$. The effect of the uncertainty on the PDF and α_s varies between ± 2 and $\pm 5\%$ and is estimated using the envelope of 52 eigenvectors of CT10NLO, and two additional PDF sets, MSTW2008NLO68CL [94] and NNPDF3.0 [68]. The impact on the background estimates in the signal region is of the order of 2-5%.

For the total cross section the impact of the theoretical uncertainties on the signal acceptance and the uncertainties on the Higgs boson branching fraction are also considered. The dominate uncertainty corresponds to the branching ratio and amounts to 2.2% [27].

6.2.2 Theoretical uncertainties on event categorisation and BSM studies

The main source of theoretical uncertainty in this analysis is given by the prediction of the ggF process in the different n-jet categories and the corresponding discriminant distributions. The ggF process is the major background in the 2-jet categories that are used to extract the measurement of the cross sections of the VBF and VH production modes. The uncertainties on the fraction of ggF events in the exclusive jet bin categories have been computed following the procedure described in Ref. [39] and updated with the latest prediction for inclusive jet cross sections and exclusive jet bin fractions [26]. The uncertainties on the cross section prediction in inclusive n-jet selections are propagated to the exclusive jet bin requirements using the expected ggF fractions keeping track of the correlation of the migrations between exclusive jet bins. The most relevant uncertainties on the shapes of the discriminants are those related to the BDTs used in the VH-hadronic and VBF 2-jet categories. These have been evaluated by taking the envelope between the QCD scale uncertainties applied to the MADGRAPH5_AMC@NLO (with the FxFx merging scheme) sample and the difference between this sample and the baseline POWHEG-BOX simulation. For the 0- and 1-jet BDT discriminants the uncertainties have been evaluated by propagating the QCD and PDF uncertainties on the baseline sample and they have a negligible impact on the final measurement. Additional uncertainties on the acceptance of the ggF process related to the QCD scale uncertainty, PDF and underlying event plus parton shower have also been included.

For the VH (with hadronic vector boson decays) and VBF production modes the two leading jets are already present in the leading order matrix element so theoretical uncertainties are expected to be much smaller then for the ggF process. Their systematics have been evaluated by varying QCD scales and applying the PDF uncertainties as for the ggF signal.

The theoretical uncertainties on the dominant ZZ^* background are evaluated following the same procedure as for the inclusive cross section described in section 6.2.1. In addition to evaluate possible migration between categories the prediction between the baseline sample POWHEG-BOX are compared with the SHERPA 2.1.1 sample which contains matrix element predictions up to three additional partons. Due to the limited statistics for the Sherpa sample in the signal region, the systematic constraints are extracted over an enlarged mass range. The fraction of events in the different categories have been compared and the relative differences are used as systematic uncertainties. In propagating them to the results, the correlations between category migrations are preserved. In addition, the yields in different jet bin categories have been compared to the data in the high mass region (above 200 GeV) and a good agreement between the SHERPA predictions and the data is found. The discriminant distributions are also compared between POWHEG-BOX and SHERPA and with the data in the high mass region. Since the observed differences are rather small and given the large data statistical uncertainties, the systematic uncertainty associated to the discriminant shapes have been considered as negligible.

Concerning the search for BSM interactions, parameterised via the effective Lagrangian terms, the theoretical uncertainties on the PDF set and the missing higher order QCD and EW corrections are in general assumed to factorize with respect to the new physics. The main sensitivity to the BSM couplings (κ_{HVV} and $\kappa_{AVV} \cdot \sin\alpha$) studied in this note comes from the VBF and VH production yields that are expected to scale as the fourth power of the BSM couplings. In Ref. [95] differences in k-factors between different BSM models and SM are shown to be in the range of $2-12\%$ for both VBF and VH processes. In addition in Ref. [95] the distributions of several kinematic quantities that affect the event categorisation, like the jet transverse momenta and the di-jet invariant mass, are shown to receive higher order corrections that can differ, depending on the value of the BSM couplings, up to 20% from those computed for the SM process. For this reason in addition to the theoretical uncertainties applied to the different signals described above,

a 30% uncertainty on the BSM signal acceptance in each category for the VH and VBF processes is also applied.

6.2.3 Theoretical uncertainties in high-mass scalar resonance search

The major source of systematics is related to the estimate of the ZZ background. In the high mass region the invariant mass spectrum for the main process ($q\bar{q}$ production) is affected by large QCD and EW corrections.

As in 6.2.1, the uncertainties on the normalisation and m_{4l} shape due to renormalisation and factorization scales uncertainty and PDF uncertainty have been considered. An additional uncertainty on possible migration between the ggF and VBF categories is considered by comparing the relative expected yields in the two categories between SHERPA and POWHEG-BOX.

In addition the subdominant gluon initiated ZZ production ($gg \rightarrow (H^*) \rightarrow ZZ$ that also includes the off-shell contribution from the SM 125 GeV Higgs boson) also contributes in a non negligible way in the high mass region. As described in Section 3, a 60% relative uncertainty on the normalisation is considered. For the high mass VBF category this uncertainty is increased to 100% .

An hypothetical high mass scalar resonance can also have interference with the continuum ZZ process and with the SM Higgs boson. These interference effects can modify the signal mass distribution, in particular if the intrinsic width of the new resonance is large. Such effects are neglected in this note.

Theory systematic uncertainties have been considered for the ggF heavy scalar contribution in the VBF category using generated events with MADGRAPH5_AMC@NLO. A 40% relative systematics uncertainty is assigned to the ggF expected fraction in the high mass VBF category.

Finally, theoretical uncertainty on the acceptance for the ggF and VBF signals due to PDF, scales and showering uncertainty, have been computed. In the ggF category the envelope of these uncertainties ranges between 1-2% for the ggF signal and 1-3% for the VBF signal. In the VBF category the envelope of these uncertainties ranges between 6-4% for the ggF signal and 2-4% for the VBF signal.

7 Results

7.1 Signal and background yields

The mass spectrum for $m_{4\ell}$ is shown for the selected events in Fig. 4 in the low mass region together with the expected ZZ^* and reducible backgrounds, and an expected SM Higgs signal at 125 GeV. Figure 4(b) shows the distribution of m_{12} versus m_{34} for the candidates with $m_{4\ell}$ within 115–130 GeV, and their projections, are shown in Figs. 4(c) and 4(d). The Z-mass constrained kinematic fit is not applied to the m_{12}, m_{34} distributions. The mass spectrum in the high mass region, both inclusively and for the ggF-enriched and VBF-enriched categories used in the analysis, is shown in Fig. 5.

The number of observed candidate events for each of the four decay channels in the mass window 118–129 GeV and the signal and background expectations are presented in Table 9.

The number of observed candidate events for each of the four decay channels in a mass spectrum above 140 GeV along with the background expectations are presented in Table 10.
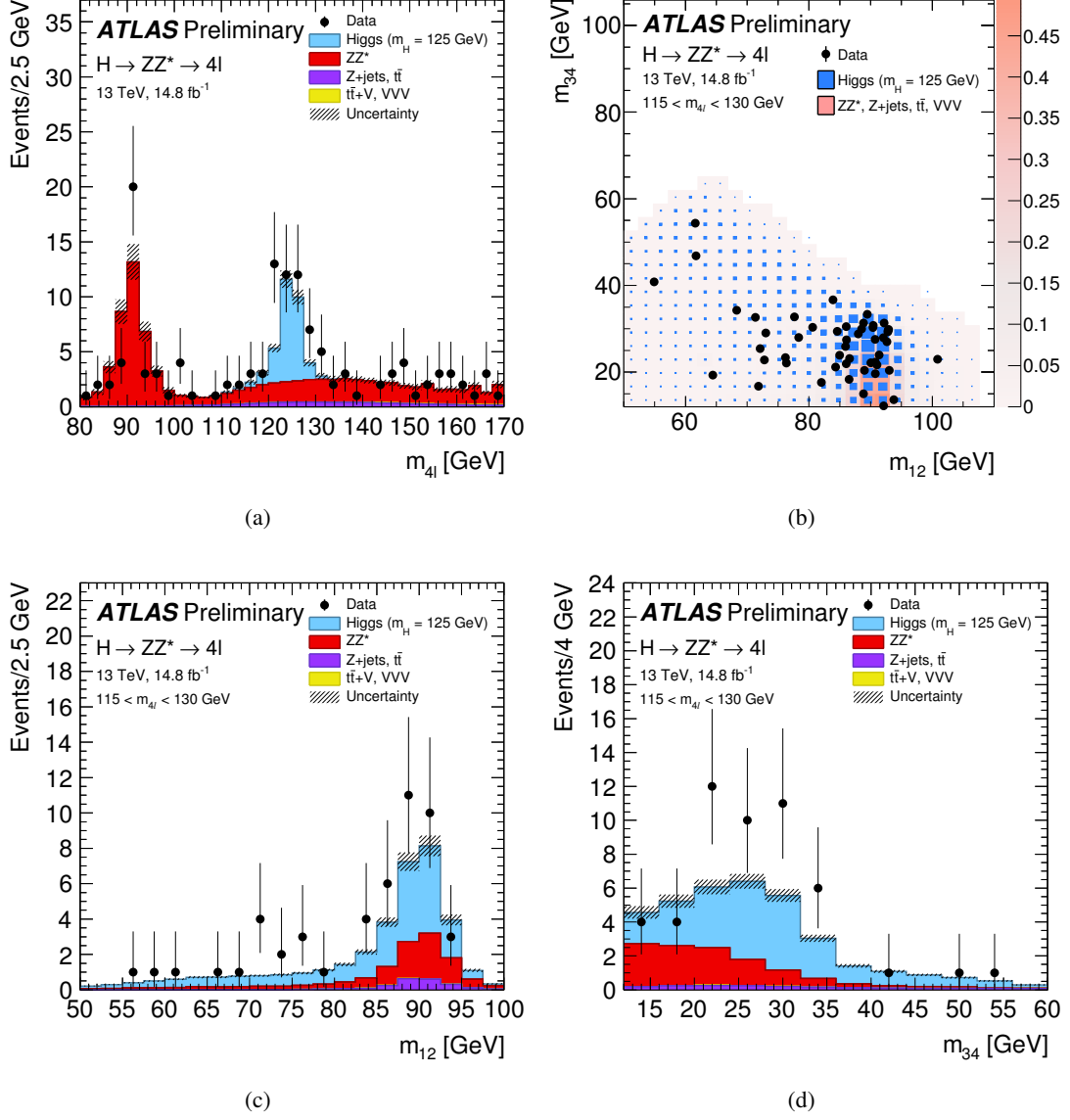
Figure 4: (a) The $m_{4\ell}$ distribution of the selected candidates, compared to the background expectation in the low mass region. (b) The distribution of data (filled circles) and the expected signal and backgrounds events in the $m_{34} - m_{12}$ plane with the requirement of $m_{4\ell}$ in 115–130 GeV . The projected distributions are shown for (c) m_{12} and (d) m_{34}. The signal contribution is shown for $m_H = 125$ GeV as blue histograms in (a), (c) and (d). The expected background contributions, ZZ^* (red histogram), $Z+$ jets plus $t\bar{t}$ (purple histogram) and $t\bar{t}V$ plus VVV (yellow histogram), are shown in (a), (c) and (d); the systematic uncertainty associated to the total signal plus background contribution is represented by the hatched areas. The expected distributions of the Higgs signal (blue) and total background (red) are superimposed in (b), where the box size (signal) and colour shading (background) represent the relative density.
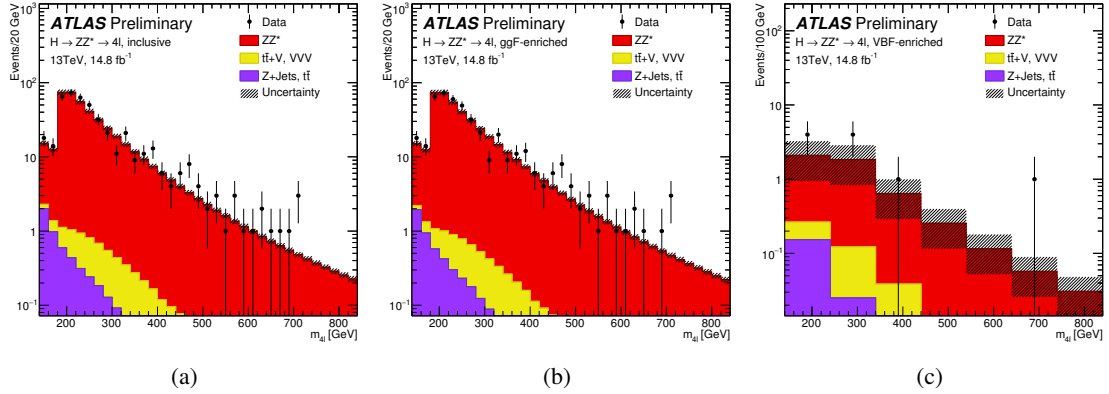
Figure 5: $m_{4\ell}$ distribution of the selected candidates, compared to the SM expectation between 140 and 840 GeV. The expected distributions of the ZZ^* background (red), the reducible background (purple) and $t\bar{t}V$ plus VVV (yellow histogram) are superimposed.

Table 9: The number of events expected and observed for a m_H=125 GeV hypothesis for the four-lepton final states. The second column gives the expected signal without any cut on $m_{4\ell}$. The other columns give for the 118–129 GeV mass range the number of expected signal events, the number of expected ZZ^* and other background events, and the signal-to-background ratio (S/B), together with the number of observed events, for 14.8 fb^{-1} at $\sqrt{s}$ = 13 TeV. Full uncertainties are provided.

Final State	Signal full mass range	Signal	ZZ^*	Z + jets, $t\bar{t}$ ttV,VVV, WZ	S/B	Expected	Observed
4μ	8.8 ± 0.6	8.2 ± 0.6	3.11 ± 0.30	0.31 ± 0.04	2.4	11.6 ± 0.7	16
$2e2\mu$	6.1 ± 0.4	5.5 ± 0.4	2.19 ± 0.21	0.30 ± 0.04	2.2	8.0 ± 0.4	12
$2\mu2e$	4.8 ± 0.4	4.4 ± 0.4	1.39 ± 0.16	0.47 ± 0.05	2.3	6.2 ± 0.4	10
$4e$	4.8 ± 0.5	4.2 ± 0.4	1.46 ± 0.18	0.46 ± 0.05	2.2	6.1 ± 0.4	6
Total	24.5 ± 1.8	22.3 ± 1.6	8.2 ± 0.8	1.54 ± 0.18	2.3	32.0 ± 1.8	44

7.2 Fiducial cross sections

The measured cross section σ_{fid} in the fiducial phase space, defined in Table 2, for each final state and the corresponding SM expectation $\sigma_{\text{fid,SM}}$ are reported in Table 11 The differences in the expected SM fiducial cross section values $\sigma_{\text{fid,SM}}$ for the different channels are due to the difference in the fiducial phase space for each final state. Two examples of the test statistics ($-2\Delta \ln L$) as a function of the fiducial and total four-lepton cross sections are shown in Figure 6.

The total fiducial cross section is obtained both as the sum of the four final states $\sigma_{\text{fid,sum}}^{4\ell}$ and by combining the four final state $\sigma_{\text{fid,comb}}^{4\ell}$. The former is more model independent since no assumption on the relative Higgs boson branching ratios in the for final states is made, but has a reduced statistical sensitivity compared to the combination. The measured total fiducial cross sections are:

$$\sigma_{\text{fid,sum}}^{4\ell} = 4.48^{+1.01}_{-0.89} \text{ fb}$$
$$\sigma_{\text{fid,comb}}^{4\ell} = 4.54^{+1.02}_{-0.90} \text{ fb}$$

(5)

Table 10: The number of expected and observed events for the four-lepton final states in a range of $m_{4\ell} > 140$ GeV, for 14.8 fb^{-1} at $\sqrt{s} = 13$ TeV. In the second column the number of expected ZZ^* events are shown, and in the third column the expected number of events for the reducible background and the $t\bar{t}V$ and triboson processes is quoted. The sum of the expected events and the observed ones are shown in the last two columns. Full uncertainties are provided.

Final state	ZZ^*	Z + jets, $t\bar{t}$, WZ	$t\bar{t}V$,VVV	Expected	Observed
4μ ggF-enriched	125 ± 10	0.95 ± 0.14	1.57 ± 0.09	127 ± 10	128
$2e2\mu$ ggF-enriched	205 ± 17	2.5 ± 0.4	2.75 ± 0.17	211 ± 17	199
$4e$ ggF-enriched	83 ± 7	1.47 ± 0.22	1.28 ± 0.08	86 ± 7	111
VBF-enriched	4.6 ± 2.8	0.18 ± 0.05	0.268 ± 0.016	5.1 ± 2.8	10
Total	418 ± 35	5.1 ± 0.7	5.87 ± 0.35	429 ± 35	448

Table 11: The measured fiducial cross section σ_{fid} in each final state and the corresponding SM expectation $\sigma_{\text{fid,SM}}$. The reported uncertainty for the measured cross sections includes the statistical and systematical component while for the SM predictions, the errors are taken from Ref. [26] .

Final state	measured σ_{fid} [fb]	$\sigma_{\text{fid,SM}}$ [fb]
4μ	$1.28^{+0.48}_{-0.40}$	$0.93^{+0.06}_{-0.08}$
$4e$	$0.81^{+0.51}_{-0.38}$	$0.73^{+0.05}_{-0.06}$
$2\mu2e$	$1.29^{+0.58}_{-0.46}$	$0.67^{+0.04}_{-0.04}$
$2e2\mu$	$1.10^{+0.49}_{-0.40}$	$0.76^{+0.05}_{-0.06}$

to be compared with the expected SM value $\sigma^{4\ell}_{\text{fid,SM}} = 3.07^{+0.21}_{-0.25}$ fb. In addition, the fiducial cross section have been also measured separately for the same- and opposite-flavour final state:

$$\sigma^{4\mu/4e}_{\text{fid,comb}} = 2.13^{+0.67}_{-0.57} \text{ fb} \qquad \sigma^{4\mu/4e}_{\text{fid,SM}} = 1.65^{+0.11}_{-0.13} \text{ fb}$$
$$\sigma^{2\ell2\ell'}_{\text{fid,comb}} = 2.35^{+0.73}_{-0.62} \text{ fb} \qquad \sigma^{2\ell2\ell'}_{\text{fid,SM}} = 1.42^{+0.10}_{-0.12} \text{ fb} \tag{6}$$

In the SM, the same- and opposite-flavour branching ratios differ by about 10% due to the presence of interference in the final state with all same-flavour leptons.

The total cross section is obtained by extrapolating the $\sigma^{4\ell}_{\text{fid}}$ to the full phase-space using the fiducial acceptance factors $\mathcal{A}$ in Table 3 and the SM branching ratio $\mathcal{B}(H \to 4\ell)$:

$$\sigma_{\text{tot}} = 81^{+18}_{-16} \text{ pb} \tag{7}$$

to be compared with the expected SM value $\sigma_{\text{tot,SM}} = 55.5^{+3.8}_{-4.4}$ pb. The compatibility between the total measured cross section and the SM prediction is at the level of 1.6 standard deviations. In all the cross section measurements presented, the dominant uncertainty is statistical.
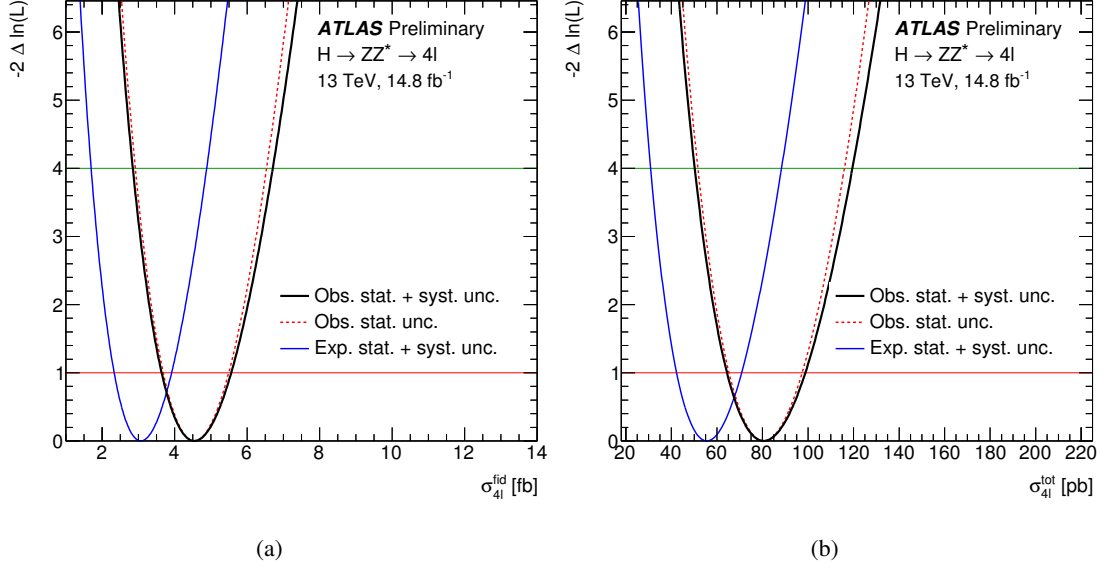
Figure 6: The values of the test statistics $-2\Delta \ln L$ as a function of (a) the fiducial cross section and (b) of the total cross section. The solid black (blue) lines shows the observed (expected SM) results including all uncertainties while the dashed red lines show the observed results without including the systematic uncertainties.

7.3 Cross sections by production mode from event categorisation

The number of expected and observed events in each of the categories, which were introduced in Section 2 and are used to enhance the sensitivity to the different Higgs boson production modes, are summarized in Table 12.

Table 12: The expected and observed yields in the 0-jet, 1-jet, 2-jet with $m_{jj} > 120$ GeV (*VBF-enriched*), 2-jet with $m_{jj} < 120$ GeV (*VH-enriched*) and VH-leptonic categories. The yields are given for the different production modes, assuming $m_H = 125$ GeV, the ZZ^* and reducible background for 14.8 fb^{-1} at $\sqrt{s} = 13$ TeV. The estimates are given for the $m_{4\ell}$ mass range 118–129 GeV. Full uncertainties are provided.

Analysis category	Signal				Background		Total expected	Observed
	ggF + $b\bar{b}H$ + $t\bar{t}H$	VBF	WH	ZH	ZZ^*	Z + jets, $t\bar{t}$		
0-jet	11.2 ± 1.4	0.120 ± 0.019	0.047 ± 0.007	0.060 ± 0.006	6.2 ± 0.6	0.84 ± 0.12	18.4 ± 1.6	21
1-jet	5.7 ± 2.4	0.59 ± 0.05	0.137 ± 0.012	0.091 ± 0.008	1.62 ± 0.21	0.44 ± 0.07	8.5 ± 2.4	12
2-jet VBF enriched	1.9 ± 0.9	0.92 ± 0.07	0.074 ± 0.007	0.052 ± 0.005	0.22 ± 0.05	0.24 ± 0.11	3.4 ± 0.9	9
2-jet VH enriched	1.1 ± 0.5	0.084 ± 0.009	0.143 ± 0.012	0.101 ± 0.009	0.166 ± 0.035	0.088 ± 0.011	1.6 ± 0.5	2
VH-leptonic	0.055 ± 0.004	< 0.01	0.067 ± 0.004	0.011 ± 0.001	0.016 ± 0.002	0.012 ± 0.010	0.16 ± 0.01	0
Total	20 ± 4	1.71 ± 0.14	0.47 ± 0.04	0.315 ± 0.027	8.2 ± 0.9	1.62 ± 0.07	32 ± 4	44

The distributions of the BDT output used in each category are shown in Fig. 8. The cross section for the different production modes are evaluated assuming the $m_H = 125.09$ GeV. Given the limited sensitivity to the $t\bar{t}H$ and $b\bar{b}H$ production mechanisms, their cross sections are evaluated together with the ggF under the assumption that the relative contribution of these production modes follows the SM prediction. Figure 9 shows the negative log-likelihood scans as function of the measured cross sections as well as

the $\sigma_{\text{ggF}+b\bar{b}H+t\bar{t}H} \cdot \mathcal{B}(H \to ZZ^*)$ versus $\sigma_{\text{VBF}+\text{VH}} \cdot \mathcal{B}(H \to ZZ^*)$. The measured values for $\sigma_{\text{ggF}+t\bar{t}H+b\bar{b}H} \cdot \mathcal{B}(H \to ZZ^*)$, $\sigma_{\text{VBF}} \cdot \mathcal{B}(H \to ZZ^*)$ and $\sigma_{VH} \cdot \mathcal{B}(H \to ZZ^*)$ with their SM expectations (on the right) are respectively:

$$
\begin{aligned}
\sigma_{\text{ggF}+b\bar{b}H+t\bar{t}H} \cdot \mathcal{B}(H \to ZZ^*) &= 1.80^{+0.49}_{-0.44} \text{ pb} & \sigma_{\text{SM,ggF}+b\bar{b}H+t\bar{t}H} \cdot \mathcal{B}(H \to ZZ^*) &= 1.31 \pm 0.07 \text{ pb} \\
\sigma_{\text{VBF}} \cdot \mathcal{B}(H \to ZZ^*) &= 0.37^{+0.28}_{-0.21} \text{ pb} & \sigma_{\text{SM,VBF}} \cdot \mathcal{B}(H \to ZZ^*) &= 0.100 \pm 0.003 \text{ pb} \\
\sigma_{\text{VH}} \cdot \mathcal{B}(H \to ZZ^*) &= 0^{+0.15} \text{ pb} & \sigma_{\text{SM,VH}} \cdot \mathcal{B}(H \to ZZ^*) &= 0.059 \pm 0.002 \text{ pb}
\end{aligned}
\tag{8}
$$

The compatibility between the measured $\sigma_{\text{ggF}+b\bar{b}H+t\bar{t}H} \cdot \mathcal{B}(H \to ZZ^*)$ and the SM prediction is at the level of 1.1 standard deviations, while for the $\sigma_{\text{VBF}} \cdot \mathcal{B}(H \to ZZ^*)$ the compatibility with the SM prediction is at the level of 1.4 standard deviations.

The cross section results by production mode from the event categorisation can also be interpreted in the LO framework [40, 96] (κ framework) in which coupling modifiers, κ_i are introduced to parameterise possible deviations from the SM predictions of the Higgs boson couplings to SM bosons and fermions. One interesting benchmark allows for two different Higgs boson coupling strength modifiers to fermions and bosons, reflecting the different structure of the interactions of the SM Higgs sector with gauge bosons and fermions. The universal coupling-strength scale factors κ_F for all fermions and κ_V for all vector bosons are defined as $\kappa_V = \kappa_W = \kappa_Z$ and $\kappa_F = \kappa_t = \kappa_b = \kappa_\tau = \kappa_g = \kappa_\mu$. The likelihood contours at 68% CL (solid line) and 95% CL (dashed line) in the $\kappa_V - \kappa_F$ plane are shown in Figure 7 (only the quadrant $\kappa_F > 0$ and $\kappa_V > 0$ is shown since this channel is not sensitive to the relative sign of the two coupling modifiers). The Higgs boson mass is assumed to be $m_H = 125.09$ GeV and no undetected or invisible Higgs boson decays is assumed to exist.
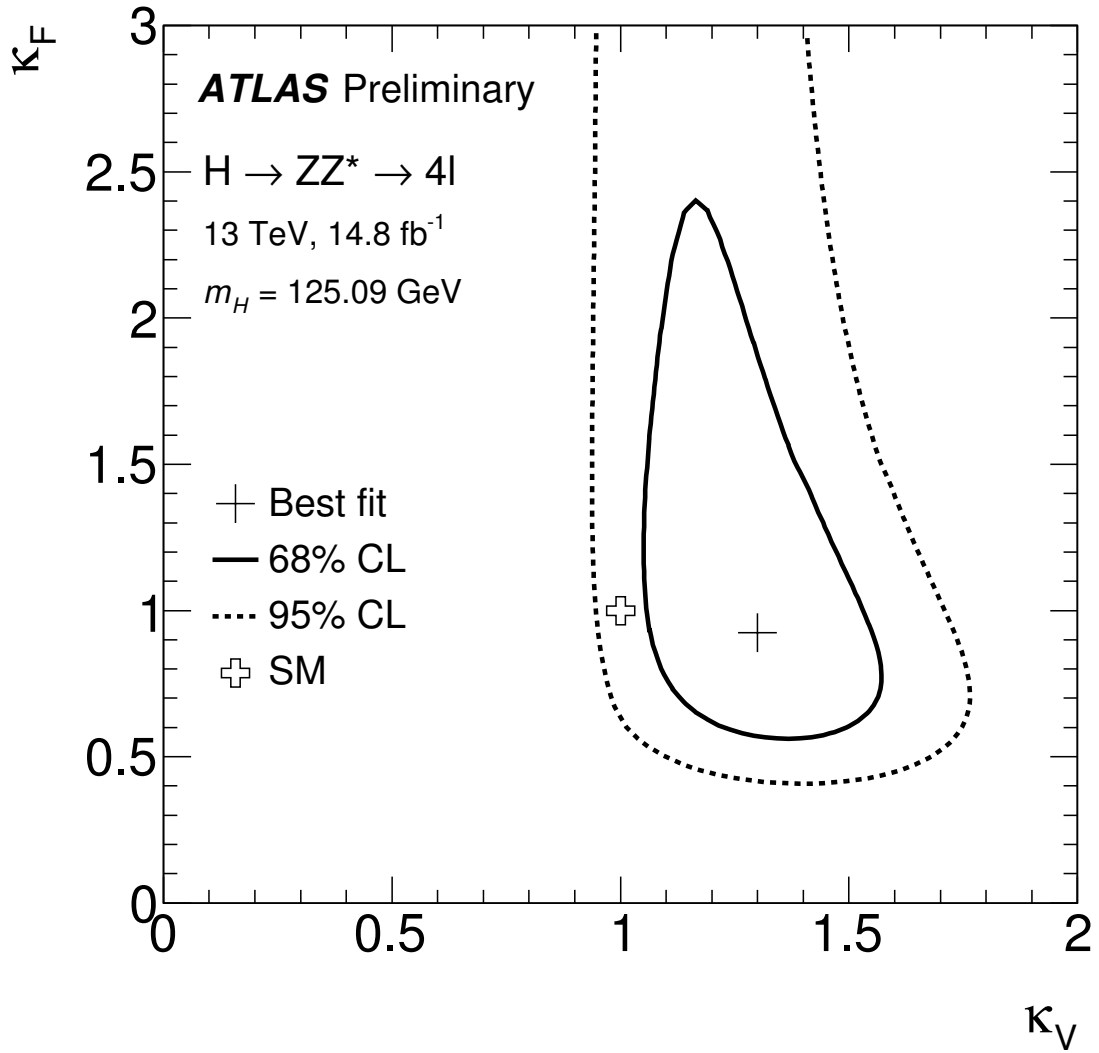
Figure 7: The likelihood contours at 68% CL (solid line) and 95% CL (dashed line) in the $\kappa_V - \kappa_F$ plane derived from the event categorisation results as described in the text (only the quadrant $\kappa_F > 0$ and $\kappa_V > 0$ is shown since this channel is not sensitive to the relative sign of the two coupling modifiers). The Higgs boson mass is assumed to be $m_H = 125.09$ GeV and no undetected or invisible Higgs boson decays is assumed to exist.

(a)

(b)

(c)

(d)
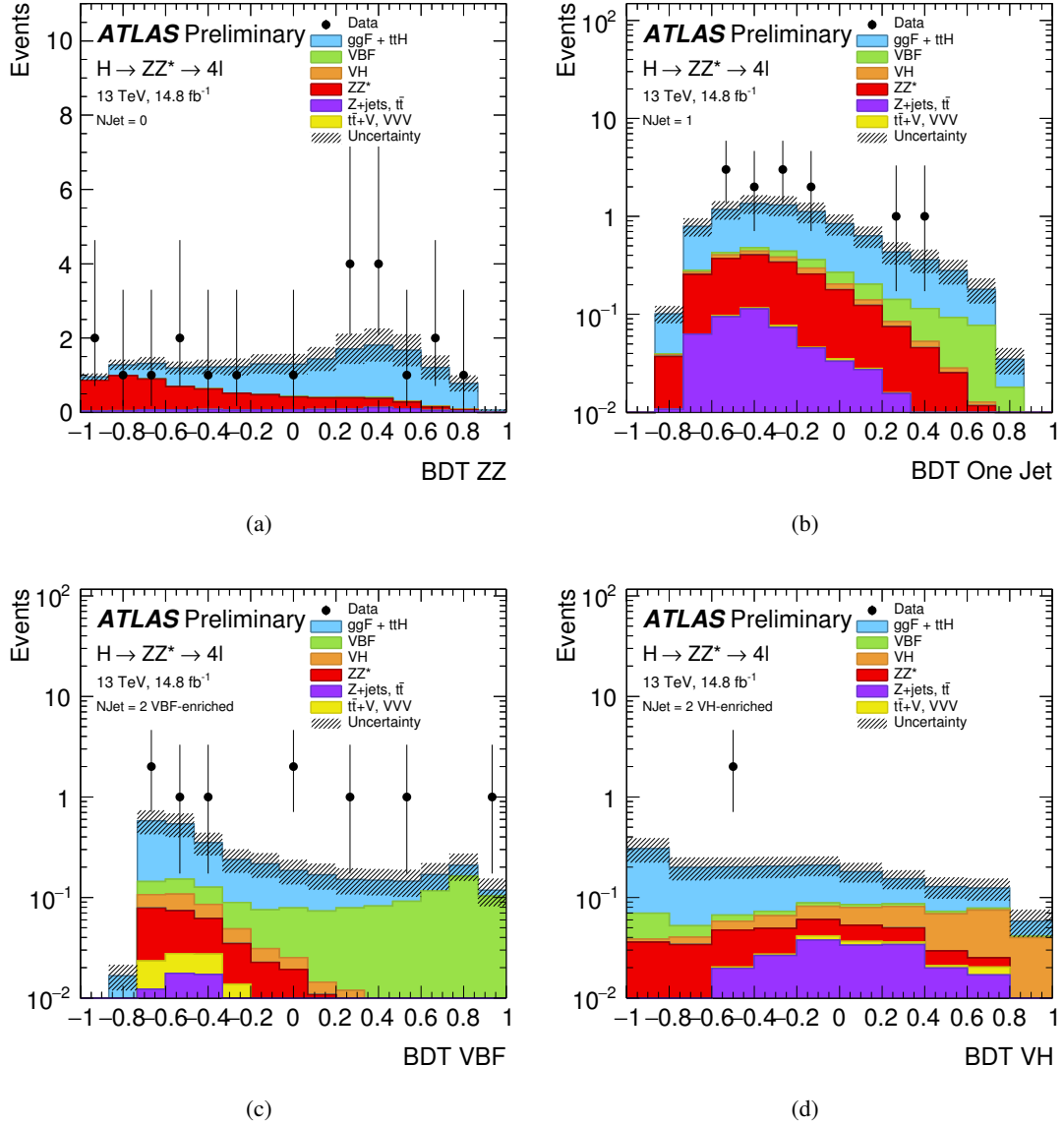
Figure 8: The distributions of the BDT output of the discriminants used in the different analysis categories for the selected events and expected signal and background yields: 0-jet (a), 1-jet (b), 2-jet VBF (c), and 2-jet VH-hadronic (d). The expected Higgs signal contributions from the ggF (blue histogram), VBF (green histogram) and VH (orange histogram) production modes are included. The expected background contributions, ZZ^* (red histogram) and $Z + jets$ plus $t\bar{t}$ (violet histogram), are also shown; the systematic uncertainty associated to the total signal plus background contribution is represented by the hatched areas.
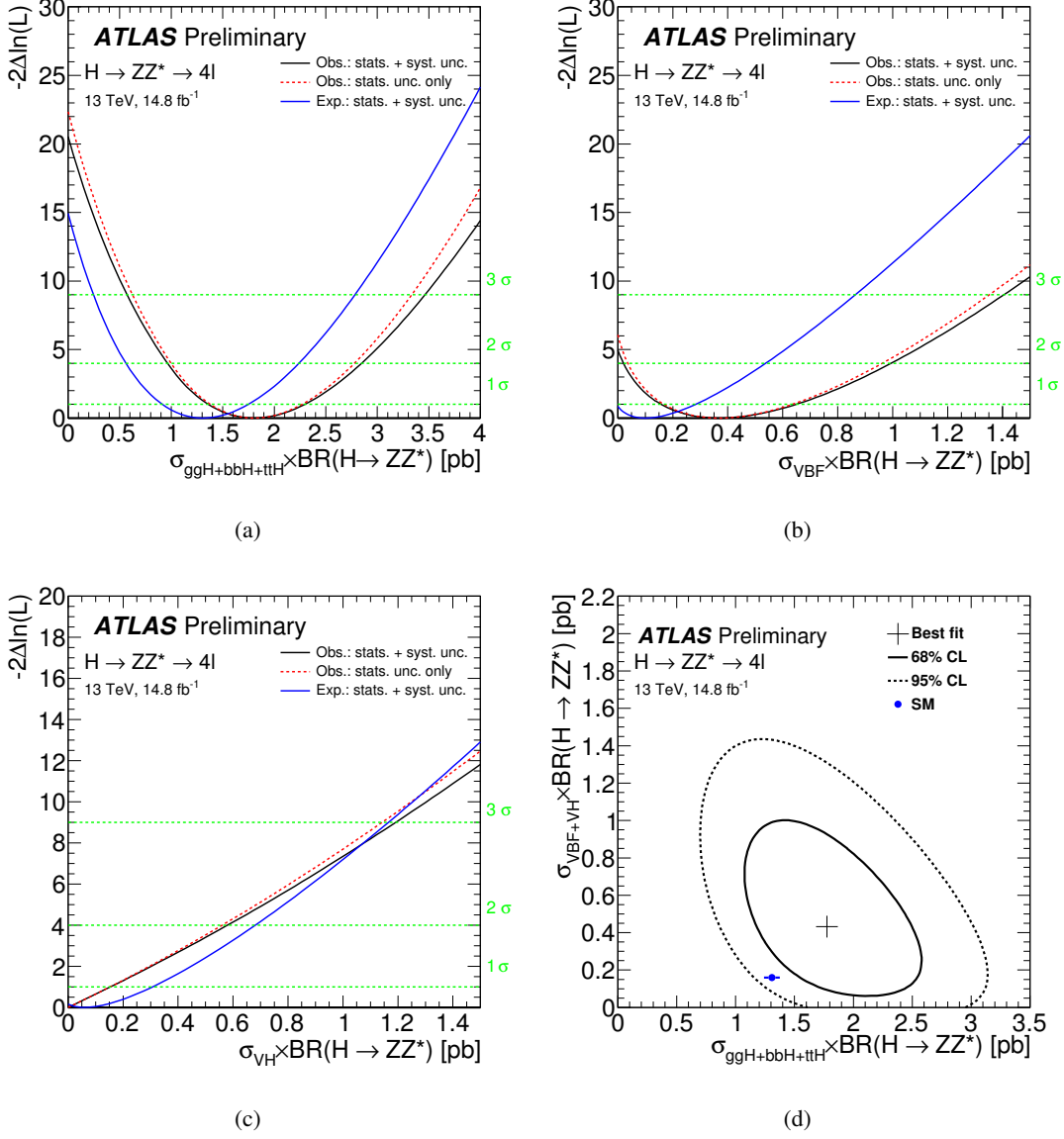
Figure 9: (a)–(c) The observed negative log-likelihood scans for $\sigma_{ggF+b\bar{b}H+t\bar{t}H} \cdot \mathcal{B}(H \to ZZ^*)$ (a), $\sigma_{VBF} \cdot \mathcal{B}(H \to ZZ^*)$ (b) and $\sigma_{VH} \cdot \mathcal{B}(H \to ZZ^*)$ (c) with (solid black line) and without (dashed red line) systematics. The expected SM negative log-likelihood scan (solid blue line) with systematics is also shown. The green horizontal lines indicate the value of the profile likelihood ratio corresponding to 1, 2 and 3 σ intervals for the parameter of interest, assuming an asymptotic χ^2 distribution for the test statistic. (d) Shows the negative log-likelihood contours at 68% (solid line) and 95% CL (dashed line) in the $\sigma_{ggF+b\bar{b}H+t\bar{t}H} \cdot \mathcal{B}(H \to ZZ^*)$ - $\sigma_{VBF+VH} \cdot \mathcal{B}(H \to ZZ^*)$ plane as well as the SM predictions (blue filled circle), with their theoretical uncertainties taken from Ref [26, 27]. The $\sigma_{VBF+VH} \cdot \mathcal{B}(H \to ZZ^*)$ is evaluated under the assumption that the relative contribution of these two production modes follows the SM prediction.

7.4 Study of BSM κ_{HVV} and $\kappa_{AVV} \cdot \sin\alpha$

Table 12 shows the comparison of the number of observed events in the different categories with the SM predictions. Limits on the BSM parameters κ_{HVV} and $\kappa_{AVV} \cdot \sin\alpha$ are derived with a fit of the yields in the categories as described in Section 2, without exploiting any additional discriminant shape information. In the fit, κ_{SM} which simply scales the SM part of the interactions, is fixed to unity. This includes the ggF production, which is fixed to the SM expectation. The decay branching fraction to ZZ^* is left free along with the value of the BSM couplings. Only one of the two BSM couplings at a time is considered. Figure 10 shows the SM expected and the observed negative log-likelihood scans as function of the BSM coupling κ_{HVV} 10(a) and $\kappa_{AVV} \cdot \sin\alpha$ 10(b). In each scan the other BSM coupling parameter is left free in the fit.

(a)   (b)
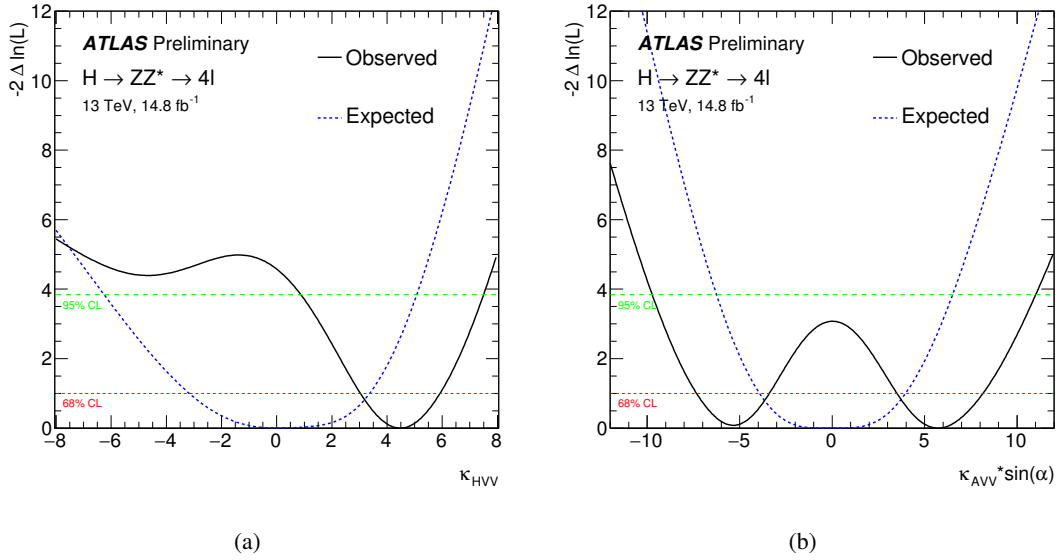
Figure 10: Observed (solid black line) and SM expected (dashed blue line) negative log-likelihood scans for κ_{HVV} (a) and $\kappa_{AVV} \cdot \sin\alpha$ (b) . The horizontal dashed lines indicate the value of the profile likelihood ratio corresponding to the 68% (red) and 95% (green) CL intervals for the parameter of interest, assuming the asymptotic χ^2 distribution of the test statistic.

In Table 13 the observed and expected limits at 95% CL for κ_{HVV} and $\kappa_{AVV} \cdot \sin\alpha$ obtained with the analysis described in this note are reported. As can be seen in Fig. 10 and Table 13, the minima of the fits are not at $\kappa_{BSM} = 0$ and the observed exclusion limits are weaker than the expected limits. This is due to the fact that the observed number of events is larger than those predicted by the SM in several categories, in particular in the *2-jet VBF enriched* category. The agreement between $\kappa_{HVV} = 0$ and the observed value is 2.1 standard deviations and between $\kappa_{AVV} \cdot \sin\alpha = 0$ and the observed value is 1.8 standard deviations. These agreements are worse than what is observed in Section 7.3, and arise for two reasons. First, in the κ_{BSM} fits the ggF production is fixed to the SM (κ_{BSM} enters only in the decay branching fraction and thus has a much smaller effect on the overall ggF rate than for the VBF and VH processes), and cannot absorb part of the excess in the 2-jet VBF enriched category as has happened for the fits reported in Section 7.3. Second, only the total yields in each category are used in this fit, while the BDT discriminant shapes are used for the results of Section 7.3.

It has to be stressed that the Run−1 results [12] cannot be directly compared with those reported in

this note. The Run−1 limits have been obtained under very different assumptions: only the kinematic properties of the four lepton decay were used to constraint the BSM couplings while the dependence of the event yields on the BSM couplings was not considered in the fit. In this analysis only the yields in categories sensitive to the production mode are used. In addition these results are obtained by fixing the SM part of the interactions while in Run−1 the ratio of the BSM coupling to the SM one was left as a free parameter.

Table 13: Observed and expected limits at 95% CL on κ_{HVV} and $\kappa_{AVV} \cdot \sin \alpha$.

Not excluded	κ_{HVV}		$\kappa_{AVV} \cdot \sin \alpha$	
range at 95% CL	expected	observed	expected	observed
	$[-6.3, 5.1]$	$[0.9, 7.5]$	$[-6.3, 6.5]$	$[-9.7, 11.0]$

7.5 Results for the heavy scalar search

The parameter of interest in the search for an additional heavy scalar is the cross section times branching ratio of heavy Higgs boson production. It is assumed that an additional scalar would be produced predominantly via the ggF and VBF processes but that the ratio of the two production mechanisms is unknown in the absence of a specific model. For this reason, fits for the ggF and VBF production processes are done separately, and in each case the other production process is left free in the fit.

The maximum deviation from the SM background hypothesis is found at a mass around 705 GeV with a narrow-width hypothesis using the inclusive analysis without ggF-VBF categories, and the corresponding local p-value is about 2.9 standard deviations. The global p-value, taking into account that such excess can happen anywhere in the mass spectrum, is about 1.9 standard deviations.

Since no significant excess in the search is found, limits on the cross section times branching ratio for an additional heavy narrow resonance are obtained as a function of m_S with the CL_s procedure in the asymptotic approximation for both ggF and VBF production modes.

Figure 11 presents the expected and observed limits at 95% confidence level on $\sigma \times \mathcal{B}(S \to ZZ \to 4\ell)$. Since this analysis assumes a narrow intrinsic width for the heavy particle, the results are valid for models in which the width is less than 0.5% of m_S.

In the mass range considered for this search the 95% confidence level (CL) upper limits on the cross section times branching ratio for heavy Higgs boson production vary between 4.6 fb at $m_S = 244$ GeV and 0.22 fb at $m_S = 1000$ GeV in the ggF channel and between 1.9 fb at $m_S = 234$ GeV and 0.2 fb at $m_S = 1000$ GeV in the VBF channel. A cross check using pseudo-experiments instead of the asymptotic approximation, results in cross section limits that are higher by not more than 25% for m_S above 550 GeV. The effect is much smaller at lower masses due to more statistics.

In the case of LWA, limits on the $\sigma_{ggF} \times \mathcal{B}(S \to ZZ \to 4\ell)$ assuming intermediate widths of the heavy scalar are also set. Figures 12(a), 12(b), 12(c) show the limits for a width of 1%, 5% and 10% of m_S, respectively. The limits are set for masses of m_S higher than 400 GeV.
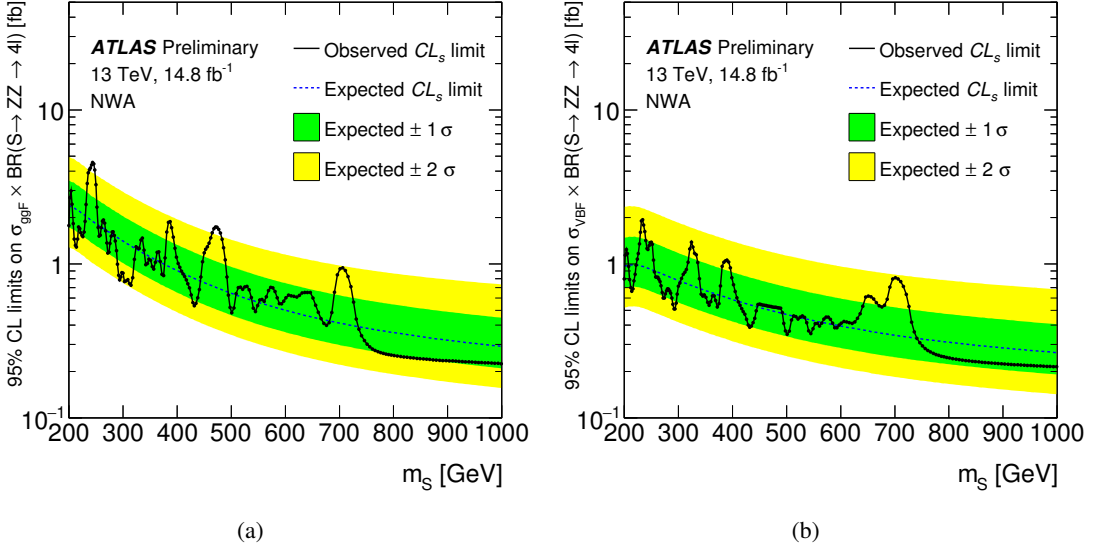
Figure 11: The 95% confidence limits on $\sigma \times \mathcal{B}(S \to ZZ \to 4\ell)$ as function of m_S for an additional narrow heavy scalar for the ggF (left) and VBF (right) production modes.

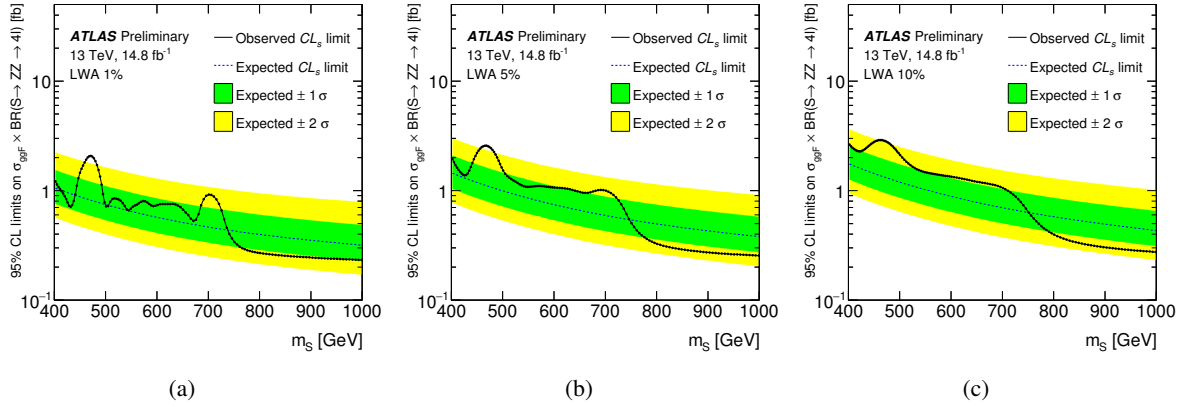Figure 12: The 95% confidence limits on $\sigma_{ggF} \times \mathcal{B}(S \to ZZ \to 4\ell)$ as function of m_S for an additional heavy scalar assuming a width of 1% (a), 5% (b), 10% (c) of m_S.

8 Conclusions

The properties of the Higgs boson resonance have been studies in the four-lepton decay channel using 14.8 fb^{-1} of integrated luminosity collected in pp collisions by the ATLAS detector at the LHC at a centre-of-mass energy of 13 TeV. The measured properties are in agreement with SM predictions in terms of fiducial and total inclusive cross sections as well as in terms of cross sections per production mode. The categories used to measure the production mode cross sections have also been used to derive limits on possible BSM interactions of the Higgs boson with the SM vector bosons in the framework of an effective Lagrangian extension of the SM.

A search for high-mass scalar resonances decaying into a four-lepton final state has also been performed

and no significant excess has been observed. Limits on the cross section times branching fractions have been derived at 95% confidence level.

References

[1] ATLAS Collaboration, *Observation of a new particle in the search for the Standard Model Higgs boson with the ATLAS detector at the LHC*, Phys. Lett. B **716** (2012) 1, arXiv: 1207.7214 [hep-ex].

[2] CMS Collaboration, *Observation of a new boson at a mass of 125 GeV with the CMS experiment at the LHC*, Phys. Lett. **B716** (2012) 30, arXiv: 1207.7235 [hep-ex].

[3] F. Englert and R. Brout, *Broken Symmetry and the Mass of Gauge Vector Mesons*, Phys. Rev. Lett. **13** (1964) 321.

[4] P. W. Higgs, *Broken Symmetries and the Masses of Gauge Bosons*, Phys. Rev. Lett. **13** (1964) 508.

[5] G. S. Guralnik, C. R. Hagen and T. W. B. Kibble, *Global Conservation Laws and Massless Particles*, Phys. Rev. Lett. **13** (1964) 585.

[6] ATLAS Collaboration, *Measurements of the Higgs boson production and decay rates and coupling strengths using pp collision data at $\sqrt{s}$ = 7 and 8 TeV in the ATLAS experiment*, Eur. Phys. J. **C76** (2016) 6, arXiv: 1507.04548 [hep-ex].

[7] CMS Collaboration, *Precise determination of the mass of the Higgs boson and tests of compatibility of its couplings with the standard model predictions using proton collisions at 7 and 8 TeV*, Eur. Phys. J. **C75** (2015) 212, arXiv: 1412.8662 [hep-ex].

[8] ATLAS Collaboration, *Evidence for the spin-0 nature of the Higgs boson using ATLAS data*, Phys. Lett. B **726** (2013) 120, arXiv: 1307.1432 [hep-ex].

[9] ATLAS and CMS Collaborations, *Combined Measurement of the Higgs Boson Mass in pp Collisions at $\sqrt{s}$ = 7 and 8 TeV with the ATLAS and CMS Experiments*, Phys. Rev. Lett. **114** (2015) 191803, arXiv: 1503.07589 [hep-ex].

[10] ATLAS and CMS Collaborations, *Measurements of the Higgs boson production and decay rates and constraints on its couplings from a combined ATLAS and CMS analysis of the LHC pp collision data at $\sqrt{s}$ = 7 and 8 TeV*, (2016), arXiv: 1606.02266 [hep-ex].

[11] ATLAS Collaboration, *Measurements of Higgs boson production and couplings in the four-lepton channel in pp collisions at center-of-mass energies of 7 and 8 TeV with the ATLAS detector*, Phys. Rev. **D91** (2015) 012006, arXiv: 1408.5191 [hep-ex].

[12] ATLAS Collaboration, *Study of the spin and parity of the Higgs boson in diboson decays with the ATLAS detector*, Eur. Phys. J. **C75** (2015) 476, arXiv: 1506.05669 [hep-ex].

[13] ATLAS Collaboration, *Fiducial and differential cross sections of Higgs boson production measured in the four-lepton decay channel in pp collisions at $\sqrt{s}$=8 TeV with the ATLAS detector*, Phys. Lett. **B738** (2014) 234, arXiv: 1408.3226 [hep-ex].

[14] ATLAS Collaboration, *Search for an additional, heavy Higgs boson in the H → ZZ decay channel at $\sqrt{s}$ = 8 TeV in pp collision data with the ATLAS detector*, Eur. Phys. J. **C76** (2016) 45, arXiv: 1507.05930 [hep-ex].

[15] ATLAS Collaboration,
Measurements of Higgs boson production cross section at 7, 8 and 13 TeV centre-of-mass energies and search for new physics at 13 TeV in the H → ZZ → 4ℓ final state with the ATLAS detector*, ATLAS-CONF-2015-059 (2015), URL: http://cdsweb.cern.ch/record/2114825.

[16] G. Branco et al., *Theory and phenomenology of two-Higgs-doublet models*, Phys. Rept. **516** (2012) 1, arXiv: 1106.0034 [hep-ph].

[17] A. Hill and J. Van Der Bij, *Strongly interacting singlet doublet Higgs model*, Phys. Rev. **D 36** (1987) 3463.

[18] ATLAS Collaboration, *The ATLAS Experiment at the CERN Large Hadron Collider*, JINST **3** (2008) S08003.

[19] ATLAS Collaboration,
Electron identification measurements in ATLAS using $\sqrt{s}$ = 13 TeV data with 50 ns bunch spacing, ATL-PHYS-PUB-2015-041, 2015, URL: http://cdsweb.cern.ch/record/2048202.

[20] ATLAS Collaboration, *Electron efficiency measurements with the ATLAS detector using the 2012 LHC proton-proton collision data*, ATLAS-CONF-2014-032 (2014), URL: http://cdsweb.cern.ch/record/1706245.

[21] ATLAS Collaboration,
Electron and photon energy calibration with the ATLAS detector using LHC Run 1 data, Eur. Phys. J. **C74** (2014) 3071, arXiv: 1407.5063 [hep-ex].

[22] ATLAS Collaboration, *Muon reconstruction performance of the ATLAS detector in proton–proton collision data at $\sqrt{s}$ =13 TeV*, Eur. Phys. J. **C76** (2016) 292, arXiv: 1603.05598 [hep-ex].

[23] M. Cacciari and G. P. Salam, *Dispelling the N^3 myth for the k_t jet-finder*, Phys. Lett. **B 641** (2006) 57, arXiv: hep-ph/0512210.

[24] M. Cacciari, G. P. Salam and G. Soyez, *The Anti-k(t) jet clustering algorithm*, JHEP **04** (2008) 063, arXiv: 0802.1189 [hep-ph].

[25] ATLAS Collaboration, *Performance of pile-up mitigation techniques for jets in pp collisions at $\sqrt{s}$ = 8 TeV using the ATLAS detector*, (2015), arXiv: 1510.03823 [hep-ex].

[26] LHC Higgs Cross Section Working Group, https://twiki.cern.ch/twiki/bin/view/LHCPhysics/CERNYellowReportPageAt13TeV.

[27] LHC Higgs Cross Section Working Group, https://twiki.cern.ch/twiki/bin/view/LHCPhysics/CERNYellowReportPageBR.

[28] G Cowan et al., *Asymptotic formulae for likelihood-based tests of new physics*, Eur. Phys. J. **C 71** (2011) 1554, arXiv: 1007.1727.

[29] A. Hoecker et al., *TMVA: Toolkit for Multivariate Data Analysis*, PoS **ACAT** (2007) 040, arXiv: physics/0703039.

[30] P. Artoisenet et al., *A framework for Higgs characterisation*, JHEP **11** (2013) 043, arXiv: 1306.6464 [hep-ph].

[31] J. Alwall et al., *The automated computation of tree-level and next-to-leading order differential cross sections, and their matching to parton shower simulations*, JHEP **07** (2014) 079, arXiv: 1405.0301 [hep-ph].

[32] S. Alioli et al., *NLO Higgs boson production via gluon fusion matched with shower in POWHEG*, JHEP **04** (2009) 002, arXiv: 0812.0578 [hep-ph].

[33] P. Nason and C. Oleari, *NLO Higgs boson production via vector-boson fusion matched with shower in POWHEG*, JHEP **02** (2010) 037, arXiv: 0911.5299 [hep-ph].

[34] T. Sjöstrand, S. Mrenna and P. Z. Skands, *A Brief Introduction to PYTHIA 8.1*, Comput. Phys. Commun. **178** (2008) 852, arXiv: 0710.3820 [hep-ph].

[35] D. J. Lange, *The EvtGen particle decay simulation package*, Nucl. Instrum. Meth. **A462** (2001) 152.

[36] R. Frederix and S. Frixione, *Merging meets matching in MC@NLO*, JHEP **12** (2012) 061, arXiv: 1209.6215 [hep-ph].

[37] M. Bahr et al., *Herwig++ Physics and Manual*, Eur. Phys. J. **C58** (2008) 639, arXiv: 0803.0883 [hep-ph].

[38] LHC Higgs Cross Section Working Group et al., *Handbook of LHC Higgs Cross Sections: 1. Inclusive Observables*, CERN-2011-002 (CERN, Geneva, 2011), arXiv: 1101.0593 [hep-ph].

[39] LHC Higgs Cross Section Working Group et al., *Handbook of LHC Higgs Cross Sections: 2. Differential Distributions*, CERN-2012-002 (CERN, Geneva, 2012), arXiv: 1201.3084 [hep-ph].

[40] LHC Higgs Cross Section Working Group et al., *Handbook of LHC Higgs Cross Sections: 3. Higgs Properties*, CERN-2013-004 (CERN, Geneva, 2013), arXiv: 1307.1347 [hep-ph].

[41] C. Anastasiou et al., *Higgs Boson Gluon-Fusion Production in QCD at Three Loops*, Phys. Rev. Lett. **114** (2015) 212001, arXiv: 1503.06056 [hep-ph].

[42] C. Anastasiou et al., *High precision determination of the gluon fusion Higgs boson cross-section at the LHC*, JHEP **05** (2016) 058, arXiv: 1602.00695 [hep-ph].

[43] S. Actis et al., *NLO electroweak corrections to Higgs boson production at hadron colliders*, Phys. Lett. **B670** (2008) 12, arXiv: 0809.1301 [hep-ph].

[44] C. Anastasiou, R. Boughezal and F. Petriello, *Mixed QCD-electroweak corrections to Higgs boson production in gluon fusion*, JHEP **04** (2009) 003, arXiv: 0811.3458 [hep-ph].

[45] M. Grazzini and H. Sargsyan, *Heavy-quark mass effects in Higgs boson production at the LHC*, JHEP **09** (2013) 129, arXiv: 1306.4581 [hep-ph].

[46] I. W. Stewart and F. J. Tackmann, *Theory uncertainties for Higgs and other searches using jet bins*, Phys. Rev. **D85** (2012) 034011, arXiv: 1107.2117 [hep-ph].

[47] M. Ciccolini, A. Denner and S. Dittmaier, *Strong and electroweak corrections to the production of Higgs + 2-jets via weak interactions at the LHC*, Phys. Rev. Lett. **99** (2007) 161803, arXiv: `0707.0381 [hep-ph]`.

[48] M. Ciccolini, A. Denner and S. Dittmaier, *Electroweak and QCD corrections to Higgs production via vector-boson fusion at the LHC*, Phys. Rev. **D77** (2008) 013002, arXiv: `0710.4749 [hep-ph]`.

[49] P. Bolzoni et al., *Higgs production via vector-boson fusion at NNLO in QCD*, Phys. Rev. Lett. **105** (2010) 011801, arXiv: `1003.4451 [hep-ph]`.

[50] O. Brein, A. Djouadi and R. Harlander, *NNLO QCD corrections to the Higgs-strahlung processes at hadron colliders*, Phys. Lett. **B579** (2004) 149, arXiv: `hep-ph/0307206 [hep-ph]`.

[51] A. Denner et al., *Electroweak corrections to Higgs-strahlung off W/Z bosons at the Tevatron and the LHC with HAWK*, JHEP **03** (2012) 075, arXiv: `1112.5142 [hep-ph]`.

[52] L. Altenkamp et al., *Gluon-induced Higgs-strahlung at next-to-leading order QCD*, JHEP **02** (2013) 078, arXiv: `1211.5015 [hep-ph]`.

[53] W. Beenakker et al., *NLO QCD corrections to t$\bar{t}$H production in hadron collisions*, Nucl. Phys. **B653** (2003) 151, arXiv: `hep-ph/0211352 [hep-ph]`.

[54] S. Dawson et al., *Associated Higgs production with top quarks at the large hadron collider: NLO QCD corrections*, Phys. Rev. **D68** (2003) 034022, arXiv: `hep-ph/0305087 [hep-ph]`.

[55] Y. Zhang et al., *QCD NLO and EW NLO corrections to t$\bar{t}$H production with top quark decays at hadron collider*, Phys. Lett. **B738** (2014) 1, arXiv: `1407.1110 [hep-ph]`.

[56] S. Frixione et al., *Electroweak and QCD corrections to top-pair hadroproduction in association with heavy bosons*, JHEP **06** (2015) 184, arXiv: `1504.03446 [hep-ph]`.

[57] S. Dawson et al., *Exclusive Higgs boson production with bottom quarks at hadron colliders*, Phys. Rev. **D69** (2004) 074027, arXiv: `hep-ph/0311067 [hep-ph]`.

[58] S. Dittmaier, M. Krämer and M. Spira, *Higgs radiation off bottom quarks at the Tevatron and the CERN LHC*, Phys. Rev. **D70** (2004) 074010, arXiv: `hep-ph/0309204 [hep-ph]`.

[59] R. V. Harlander and W. B. Kilgore, *Higgs boson production in bottom quark fusion at next-to-next-to leading order*, Phys. Rev. **D68** (2003) 013001, arXiv: `hep-ph/0304035 [hep-ph]`.

[60] A. Djouadi, J. Kalinowski and M. Spira, *HDECAY: A Program for Higgs boson decays in the Standard Model and its supersymmetric extension*, Comput. Phys. Commun. **108** (1998) 56, arXiv: `hep-ph/9704448 [hep-ph]`.

[61] A. Djouadi, M. M. Mühlleitner and M. Spira, *Decays of supersymmetric particles: The Program SUSY-HIT (SUspect-SdecaY-Hdecay-InTerface)*, Acta Phys. Polon. **B38** (2007) 635, arXiv: `hep-ph/0609292 [hep-ph]`.

[62] A. Bredenstein et al., *Precise predictions for the Higgs-boson decay H → WW/ZZ → 4 leptons*, Phys. Rev. **D74** (2006) 013004, arXiv: `hep-ph/0604011 [hep-ph]`.

[63] A. Bredenstein et al., *Radiative corrections to the semileptonic and hadronic Higgs-boson decays* $H \to WW/ZZ \to 4$ *fermions*, JHEP **02** (2007) 080, arXiv: `hep-ph/0611234 [hep-ph]`.

[64] S. Boselli et al., *Higgs boson decay into four leptons at NLOPS electroweak accuracy*, JHEP **06** (2015) 023, arXiv: `1503.07394 [hep-ph]`.

[65] J. Butterworth et al., *PDF4LHC recommendations for LHC Run II*, J. Phys. **G43** (2016) 023001, arXiv: `1510.03865 [hep-ph]`.

[66] S. Dulat et al., *New parton distribution functions from a global analysis of quantum chromodynamics*, Phys. Rev. **D93** (2016) 033006, arXiv: `1506.07443 [hep-ph]`.

[67] L. A. Harland-Lang et al., *Parton distributions in the LHC era: MMHT 2014 PDFs*, Eur. Phys. J. **C75** (2015) 204, arXiv: `1412.3989 [hep-ph]`.

[68] R. D. Ball et al., *Parton distributions for the LHC Run II*, JHEP **04** (2015) 040, arXiv: `1410.8849 [hep-ph]`.

[69] H.-L. Lai et al., *New parton distributions for collider physics*, Phys. Rev. **D82** (2010) 074024, arXiv: `1007.2241 [hep-ph]`.

[70] ATLAS Collaboration, *Measurement of the Z/γ^* boson transverse momentum distribution in pp collisions at* $\sqrt{s} = 7$ *TeV with the ATLAS detector*, JHEP **1409** (2014) 145, arXiv: `1406.3660 [hep-ex]`.

[71] F. Cascioli et al., *ZZ production at hadron colliders in NNLO QCD*, Phys. Lett. **B735** (2014) 311, arXiv: `1405.2219 [hep-ph]`.

[72] M. Grazzini, S. Kallweit and D. Rathlev, *ZZ production at the LHC: fiducial cross sections and distributions in NNLO QCD*, Phys. Lett. **B750** (2015) 407, arXiv: `1507.06257 [hep-ph]`.

[73] B. Biedermann et al., *Electroweak corrections to pp $\to \mu^+\mu^- e^+e^- + X$ at the LHC: a Higgs background study*, Phys. Rev. Lett. **116** (2016) 161803, arXiv: `1601.07787 [hep-ph]`.

[74] T. Gleisberg et al., *Event generation with SHERPA 1.1*, JHEP **02** (2009) 007, arXiv: `0811.4622 [hep-ph]`.

[75] N. Kauer, C. O'Brien and E. Vryonidou, *Interference effects for H $\to$ W W $\to \ell\nu q\bar{q}'$ and H $\to$ ZZ $\to \ell\bar{\ell}q\bar{q}$ searches in gluon fusion at the LHC*, JHEP **10** (2015) 074, arXiv: `1506.01694 [hep-ph]`.

[76] F. Caola et al., *QCD Corrections to ZZ Production in Gluon Fusion at the LHC*, Phys. Rev. **D92** (2015) 094028, arXiv: `1509.06734 [hep-ph]`.

[77] J. M. Campbell et al., *Two Loop Correction to Interference in gg $\to$ ZZ*, (2016), arXiv: `1605.01380 [hep-ph]`.

[78] K. Melnikov and M. Dowling, *Production of two Z-bosons in gluon fusion in the heavy top quark approximation*, Phys. Lett. **B744** (2015) 43, arXiv: `1503.01274 [hep-ph]`.

[79] C. S. Li et al., *Soft gluon resummation in the signal-background interference process of gg($\to h^*$)$\to$ ZZ*, JHEP **08** (2015) 065, arXiv: `1504.02388 [hep-ph]`.

[80] T. Gleisberg and S. Höche, *Comix, a new matrix element generator*, JHEP **0812** (2008) 039, arXiv: 0808.3674 [hep-ph].

[81] F. Cascioli, P. Maierhofer and S. Pozzorini, *Scattering Amplitudes with Open Loops*, Phys. Rev. Lett. **108** (2012) 111601, arXiv: 1111.5206 [hep-ph].

[82] S. Schumann and F. Krauss,
A Parton shower algorithm based on Catani-Seymour dipole factorisation,
JHEP **0803** (2008) 038, arXiv: 0709.1027 [hep-ph].

[83] S. Höche et al., *QCD matrix elements + parton showers: The NLO case*, JHEP **04** (2013) 027, arXiv: 1207.5030 [hep-ph].

[84] T. Sjöstrand, S. Mrenna and P. Z. Skands, *PYTHIA 6.4 Physics and Manual*, JHEP **05** (2006) 026, arXiv: hep-ph/0603175.

[85] ATLAS Collaboration, *The ATLAS simulation Infrastructure*, Eur. Phys. J. **C 70** (2010) 823, arXiv: 1005.4568 [physics.ins-det].

[86] S. Agostinelli et al., *GEANT4: A simulation toolkit*, Nucl. Instrum. Meth. **A 506** (2003) 250.

[87] K. S. Cranmer, *Kernel estimation in high-energy physics*,
Comput. Phys. Commun. **136** (2001) 198, arXiv: hep-ex/0011057 [hep-ex].

[88] ATLAS Collaboration,
A morphing technique for signal modelling in a multidimensional space of coupling parameters,
(2015), URL: http://cdsweb.cern.ch/record/2066980.

[89] ATLAS Collaboration,
Electron and photon energy calibration with the ATLAS detector using LHC Run 1 data,
Eur. Phys. J. **C74** (2014) 3071, arXiv: 1407.5063 [hep-ex].

[90] ATLAS Collaboration, *Jet energy measurement and its systematic uncertainty in proton-proton collisions at $\sqrt{s}$ = 7 TeV with the ATLAS detector*, Eur. Phys. J. **C75** (2015) 17, arXiv: 1406.0076 [hep-ex].

[91] ATLAS Collaboration, *Jet Calibration and Systematic Uncertainties for Jets Reconstructed in the ATLAS Detector at $\sqrt{s}$ = 13 TeV*, (2015), URL: http://cdsweb.cern.ch/record/2037613.

[92] ATLAS Collaboration, *Improved luminosity determination in pp collisions at sqrt(s) = 7 TeV using the ATLAS detector at the LHC*, Eur. Phys. J. **C73** (2013) 2518, arXiv: 1302.4393 [hep-ex].

[93] ATLAS Collaboration, *Improved luminosity determination in pp collisions at sqrt(s) = 7 TeV using the ATLAS detector at the LHC*, Eur. Phys. J. **C73** (2013) 2518, arXiv: 1302.4393 [hep-ex].

[94] A. D. Martin et al., *Parton distributions for the LHC*, Eur. Phys. J. **C63** (2009) 189, arXiv: 0901.0002 [hep-ph].

[95] F. Maltoni, K. Mawatari and M. Zaro, *Higgs characterisation via vector-boson fusion and associated production: NLO and parton-shower effects*, Eur. Phys. J. **C74** (2014) 2710, arXiv: 1311.1829 [hep-ph].

[96] LHC Higgs Cross Section Working Group,
https://twiki.cern.ch/twiki/bin/view/LHCPhysics/LHCHXSWG2KAPPA.
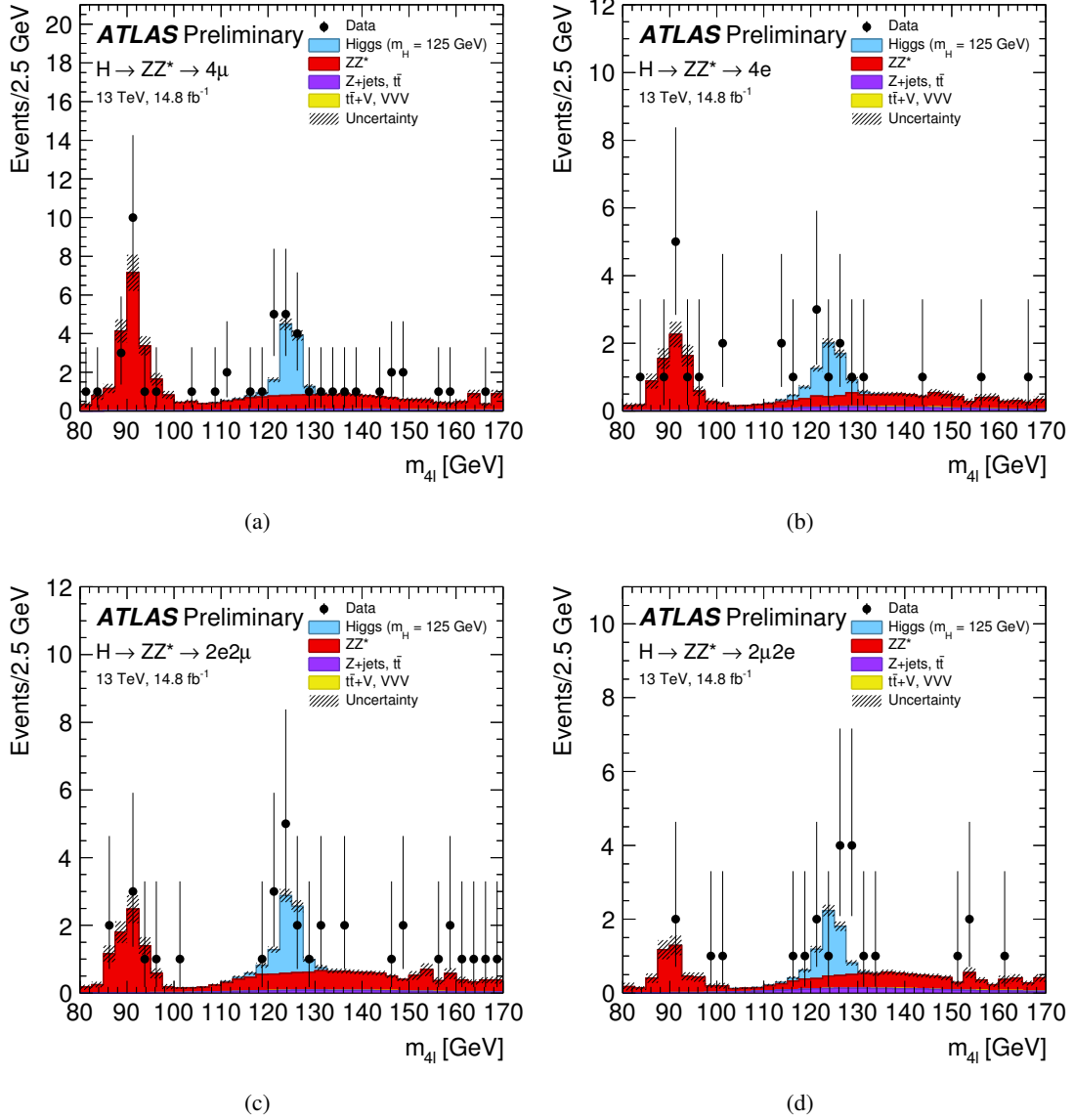
Appendix

Figure 13: The distribution of the four-lepton invariant mass, $m_{4\ell}$, for the selected candidates in the four final state (a) 4μ, (b) $4e$, (c) $2e2\mu$, (d) $2\mu2e$ for the $m_{4\ell}$ range 80-170 GeV. The signal contribution is shown for $m_H = 125$ GeV as blue histograms while the expected background contributions, ZZ^* $Z+$ jets plus $t\bar{t}$ and $t\bar{t}V$ plus VVV as red, purple and yellow histogram, respectively. The systematic uncertainty associated to the total signal plus background contribution is represented by the hatched areas.

The mass spectrum for $m_{4\ell}$ with $BDT_{ZZ} > 0$ cut is shown in Figure 14 for the low mass regions with the expected reducible and irreducible backgrounds and an expected SM Higgs signal at 125 GeV superimposed. The corresponding plots for the individual channels is given in Figure 15.
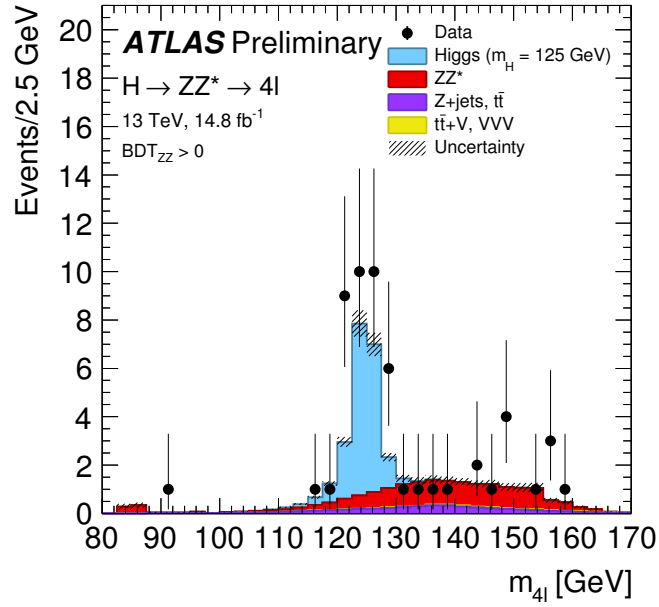

Figure 14: m_{4l} distribution of the selected candidates, compared to the background expectation. The signal expectation for $m_H = 125$ GeV is also shown.
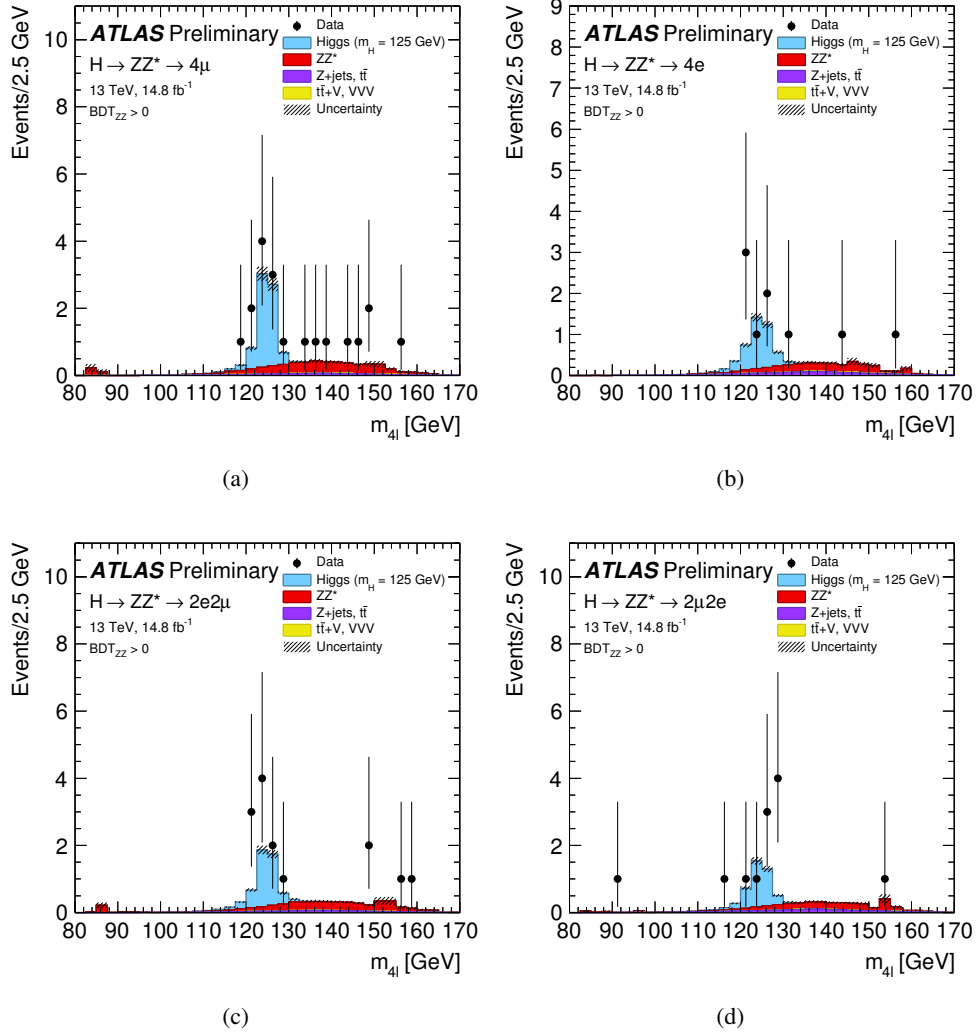
(a)

(b)

(c)

(d)

Figure 15: m_{4l} distribution with $\text{BDT}_{ZZ} > 0$ of the selected candidates, compared to the background expectation: (a) 4μ, (b) $4e$, (c) $2e2\mu$, (d) $2\mu2e$. The signal expectation for $m_H = 125$ GeV is also shown.
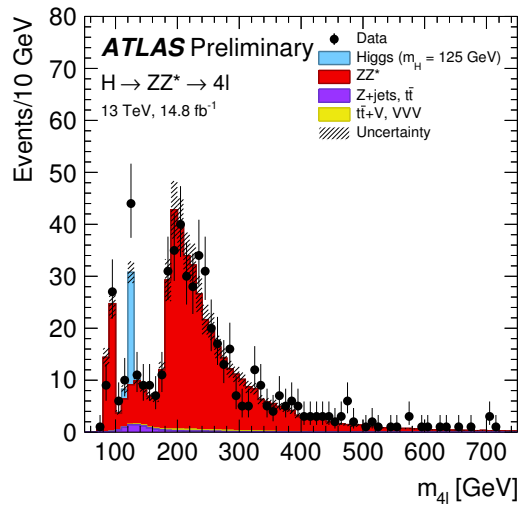
Figure 16: The distribution of the four-lepton invariant mass, $m_{4\ell}$, for the selected candidates in the signal region. The signal contribution is shown for $m_H = 125$ GeV as blue histograms while the expected background contributions, ZZ^* $Z+$ jets plus $t\bar{t}$ and $t\bar{t}V$ plus VVV as red, purple and yellow histogram, respectively. The systematic uncertainty associated to the total signal plus background contribution is represented by the hatched areas.